

Scatter in Sunyaev–Zel’dovich effect scaling relations explained by inter-cluster variance in mass accretion histories

Sheridan B. Green,¹[★]† Han Aung,¹ Daisuke Nagai,^{1,2} and Frank C. van den Bosch^{1,2}

¹*Department of Physics, Yale University, P.O. Box 208120, New Haven, CT 06520, U.S.A.*

²*Department of Astronomy, Yale University, P.O. Box 208101, New Haven, CT 06520, U.S.A.*

ABSTRACT

The X-ray and microwave observable-mass scaling relations of galaxy clusters are immensely valuable tools for cosmological analysis, but their power is currently limited by astrophysical systematic uncertainties that bias cluster mass estimates and introduce additional scatter. Turbulent energy injected into the intracluster medium via mass assembly contributes substantially to the cluster’s non-thermal pressure support, which is a significant source of such uncertainties. We use a simple analytical model to compute the mass assembly-driven non-thermal pressure profiles of individual haloes based on Monte Carlo-generated halo assembly histories from extended Press–Schechter theory. After combining this with the Komatsu–Seljak model for the total pressure to obtain thermal pressure profiles, we predict deviations from self-similarity and the intrinsic scatter in the Sunyaev–Zel’dovich effect observable-mass scaling relation ($Y_{\text{SZ}} - M$) due solely to inter-cluster variations in halo mass assembly histories. We study the dependence of the slope, normalization, and scatter of $Y_{\text{SZ}} - M$ on aperture radius, cosmology, redshift, and halo mass limit. The model predicts 5 – 9% scatter in $Y_{\text{SZ}} - M$ at $z = 0$, increasing as the aperture used to compute Y_{SZ} increases from r_{500c} to $5r_{500c}$. The predicted scatter lies slightly below that of studies based on non-radiative hydrodynamical simulations, illustrating that assembly history variance alone is likely to be responsible for a substantial fraction of the scatter in $Y_{\text{SZ}} - M$. As redshift increases, $Y_{\text{SZ}} - M$ deviates more from self-similarity and scatter increases. Lastly, we show that the residuals of $Y_{\text{SZ}} - M$ correlate strongly with the recent halo mass accretion rate, potentially providing an opportunity to infer the latter.

Key words: methods: analytical – galaxies: clusters: general – galaxies: clusters: intracluster medium – cosmology: observations

1 INTRODUCTION

Galaxy clusters are the largest gravitationally bound objects in the Universe, forming hierarchically through accretion at the intersection of cosmic filaments. Their mass- and redshift-distribution is intimately connected to the underlying cosmological model. Hence, a precise approach to linking cluster observables (such as X-ray luminosity or the Sunyaev & Zeldovich (SZ; 1972) effect in the microwave) to the underlying halo mass is essential for using cluster counts as a cosmological probe (Allen et al. 2011; Pratt et al. 2019, for a recent review).

In the upcoming years, the observed X-ray and SZ cluster samples are forecast to grow tremendously. In the X-ray, the recently-launched *eROSITA* mission is set to discover $\gtrsim 10^6$ groups and clusters (Pillepich et al. 2018). In the microwave, the Simons Ob-

servatory — planned to begin observations in the early 2020s — will detect the SZ signal of $\gtrsim 10^5$ clusters out to high redshifts (Ade et al. 2019), a catalog that will eventually be augmented to $\gtrsim 10^6$ objects by the next-generation CMB-S4 project (Abazajian et al. 2019). The statistical precision of these surveys will enable unprecedentedly tight cosmological constraints, further stress-testing the standard model of cosmology and potentially illuminating the signal of massive neutrinos or dynamical dark energy. Unlocking the full statistical potential of these surveys necessitates the mitigation of systematic uncertainties associated with cluster gas physics, motivating the development of low-scatter halo mass proxies that are accurate to the percent level.

The X-ray luminosity, L_X , is a direct, low-cost mass estimator, but it suffers from high intrinsic scatter due to poorly-understood cluster core physics. This scatter can be reduced via core-excision (Maughan 2007; Mantz et al. 2018) or modeling (Käfer et al. 2019) at the cost of sacrificing a significant fraction of the total X-ray photon distribution that comes from the cluster core regions. The

★ E-mail: sheridan.green@yale.edu (SBG)

† NSF Graduate Research Fellow

integrated SZ signal, Y_{SZ} , is predicted to have a low intrinsic scatter (10–15% at fixed mass, e.g., Nagai 2006; Battaglia et al. 2012) and is much less sensitive to cluster core physics, as the SZ signal arises from the gas permeating throughout the virialized region of galaxy clusters. The product of the X-ray core-excised spectral temperature and gas mass, Y_X , has comparable scatter to Y_{SZ} (Kraivtsov et al. 2006), but is only obtainable with high-resolution, long-exposure observations of massive, nearby clusters. Both X-ray and SZ mass proxies are also subject to scatter due to inter-cluster variance in halo mass accretion histories (MAHs; e.g., Hoekstra et al. 2012; Barnes et al. 2017b), which results in the presence of varying levels of non-thermal pressure support (Lau et al. 2009; Nelson et al. 2014b). However, the X-ray signal is further afflicted by gas clumping (e.g., Nagai & Lau 2011; Zhuravleva et al. 2013; Khedekar et al. 2013), temperature inhomogeneities (e.g., Rasia et al. 2014), and the cluster dynamical state (e.g., Ventimiglia et al. 2008), whereas the SZ signal is expected to be less sensitive to these details (e.g., Motl et al. 2005; Wik et al. 2008; Eckert et al. 2015, but see also Marrone et al. 2012). Recent machine learning-based efforts have illustrated that the scatter can be reduced by accounting for the dynamical state via full X-ray images (Ntampaka et al. 2019) or summary statistics of the cluster morphology (Green et al. 2019).

In addition to introducing scatter, non-thermal pressure support is responsible for a substantial bias that adversely impacts X-ray- and SZ-based mass proxies. These masses are typically estimated under the assumption of hydrostatic equilibrium (HSE) between the gravitational potential and the observed thermal pressure, which is used in lieu of the total pressure. Because of this assumption, the presence of non-thermal pressure in the cluster introduces a HSE mass bias, resulting in observed X-ray/SZ-based masses that are up to 30% lower than the corresponding gravitational lensing-based masses (e.g., Zhang et al. 2010; Mahdavi et al. 2013; von der Linden et al. 2014; Applegate et al. 2014; Hoekstra et al. 2015; Medezinski et al. 2018; Miyatake et al. 2019). Recent observational studies, however, have shown that this bias is much lower for relaxed populations of clusters that have not recently experienced a significant merger event (e.g., Applegate et al. 2016; Eckert et al. 2019; Ettori et al. 2019; Ghirardini et al. 2019). Hydrodynamical cosmological simulations have also found HSE biases of 5–40% (e.g., Rasia et al. 2006; Nagai et al. 2007; Lau et al. 2009; Battaglia et al. 2012; Lau et al. 2013; Nelson et al. 2014a; Shi et al. 2016; Biffi et al. 2016; Henson et al. 2017; Ansarifard et al. 2019; Barnes et al. 2020), revealing that bulk and turbulent intracluster gas motions driven by halo mergers and accretion are likely the dominant source of non-thermal pressure (e.g., Nelson et al. 2012; Avestruz et al. 2016; Shi et al. 2018, 2020) (the potential implications of other sources are discussed in Section 4). Measurements of optical weak lensing masses via background galaxies (e.g., Dietrich et al. 2019) and CMB lensing masses (e.g., Raghunathan et al. 2019) may provide a method of calibrating the cluster mass scales and mitigating the HSE bias problem.

As we approach the low-noise, high-resolution frontier of CMB survey science (Mroczkowski et al. 2019), the SZ effect offers promising potential as a cosmological probe. In contrast to X-ray mass proxies, the SZ-based approach suffers from fewer astrophysical systematics and has greater sensitivity to high-redshifts and cluster outskirts. However, as discussed above, assembly-driven non-thermal pressure support is a dominant systematic impeding SZ science. Hydrodynamical simulations demonstrate that the cluster outskirts, which contribute the majority of the thermal SZ (tSZ) signal, have non-thermal pressure support similar in magnitude to the thermal pressure (e.g., Nelson et al. 2014b; Vazza et al. 2018;

Walker et al. 2019, for a recent review). In addition to contributing to the scatter and bias in Y_{SZ} -based mass estimation, non-thermal pressure also impacts the tSZ angular power spectrum, C_l , which is extremely sensitive to the matter density fluctuation amplitude, $C_l \propto \sigma_8^{7-8}$ (Komatsu & Seljak 2002). Simulation studies have demonstrated that properly accounting for non-thermal pressure can change the SZ power spectrum amplitude by $\sim 60\%$ (Battaglia et al. 2010; Shaw et al. 2010; Trac et al. 2011), impacting constraints on σ_8 and dark energy (Bolliet et al. 2018). Cross-correlation analyses of SZ, lensing, and galaxy surveys have also been used to constrain the HSE mass bias (e.g., Makiya et al. 2018, 2019; Osato et al. 2020) as well as the roles of AGN feedback and non-thermal pressure of the warm-hot diffuse baryons in groups and clusters (e.g., Van Waerbeke et al. 2014; Battaglia et al. 2015; Hojjati et al. 2017; Osato et al. 2018). Hence, accurately characterizing the average non-thermal pressure profile as a function of cluster mass and redshift is crucial for both subjugating the HSE mass bias problem and using auto- and cross-correlation statistics from upcoming SZ surveys for cosmology. In addition, studying how diversity in halo assembly drives the scatter in the non-thermal pressure support and SZ signal may inform techniques for constructing a more powerful, lower-scatter SZ-based mass proxy that could ultimately strengthen next-generation cosmological analyses.

In this paper, we study analytically the impact of structure formation-generated turbulence on the scatter in the SZ effect observable-mass scaling relation ($Y_{\text{SZ}} - M$). This is made possible by combining the Komatsu & Seljak (2001) model of the cluster total pressure and gas density profiles, the Shi & Komatsu (2014) analytical model of the mass assembly-driven non-thermal pressure profiles, and both average halo MAHs (van den Bosch et al. 2014) and individual Monte Carlo-generated MAHs (Parkinson et al. 2008). Along the way, we identify a near-universality of the average non-thermal pressure fraction profiles $f_{\text{nth}}(r)$ at fixed peak height that was first hinted at in the simulations of Nelson et al. (2014b). We then calculate the impact of mass assembly on the HSE mass bias, finding that the average bias should increase considerably with both halo mass and redshift due to larger rates of recent mass accretion. Using the thermal pressure profiles computed for various cluster samples, we investigate the slope, normalization, and intrinsic scatter of the $Y_{\text{SZ}} - M$ relation and its dependence on aperture radius, redshift, cosmology, and halo mass limit. Importantly, we show that a substantial fraction of the scatter seen in simulated and observed $Y_{\text{SZ}} - M$ relations can be attributed to inter-cluster variance in the MAHs. Lastly, we identify a strong correlation between the $Y_{\text{SZ}} - M$ residuals and the recent halo mass accretion rate over the previous dynamical time, a relationship that may enable estimation of the accretion rate in observed clusters.

This paper is organized as follows. In Section 2, we describe our methodology, briefly reviewing models of the cluster gas and thermal pressure profiles and the MAHs as well as defining our observables of interest. In Section 3, we lay out the results of our analyses, including the predictions for cluster non-thermal pressure profiles (Section 3.1), HSE mass biases (Section 3.2), observable-mass relationships (Section 3.3), and the connection between $Y_{\text{SZ}} - M$ residuals and the recent halo mass accretion rate (Section 3.4). We discuss the implications of the model in Section 4, concluding with a summary of our findings and a forecast of future work in Section 5.

The fiducial cosmology used throughout this work is consistent with the Planck Collaboration et al. (2018) results: $\Omega_m = 0.311$, $\Omega_\Lambda = 0.689$, $\Omega_b h^2 = 0.0224$, $h = 0.677$, $\sigma_8 = 0.810$, and $n_s = 0.967$. The base-10 logarithm is denoted by \log and the nat-

ural logarithm is denoted by \ln . Much of the analysis utilizes the `coLOSSUS` Python package (Diemer 2018).

2 METHODS

In this section, we first present our theoretical model of the observable-mass scaling relations (Section 2.1), which is based on the Kaiser (1986) self-similar model. The cluster observables considered in this study are all functions of the gas density, temperature, and thermal pressure in the intracluster medium (ICM). We assume that the gas density and *total* pressure are well-described by the model of Komatsu & Seljak (2001), which we present in Section 2.2. The thermal pressure is obtained from the total by subtracting off the non-thermal component, which we compute using the model of Shi & Komatsu (2014), presented in Section 2.3. Throughout we assume that the non-thermal pressure is entirely due to turbulence generated during the cluster’s mass assembly. Hence, in Section 2.4, we describe the techniques used to compute MAHs for both the average cluster as well as for large populations of individual clusters. Lastly, we lay out our methods used to compute and quantify the properties of cluster scaling relations in Section 2.5.

2.1 Observables and self-similar scaling relations

Our main goal is to model the scaling relation between the observable, cylindrically-integrated SZ signal, Y_{SZ} , and the observationally inferred cluster mass. As discussed below, the SZ signal is proportional to both the cluster gas mass M_{gas} and the gas mass-weighted temperature T_{mg} . We therefore also analyze the scaling relations between these quantities and cluster mass. We study the dependence of all of these scaling relations on the aperture radius r_{ap} , for which we use multiples of r_{500c} and r_{200m} .¹ In what follows, we use R to denote two-dimensional projected distances and r to denote three-dimensional distances; in particular, R_{ap} and r_{ap} are used to indicate the aperture radii used for cylindrically- and spherically-integrated quantities, respectively. The total enclosed halo mass is denoted $M(< r_{\text{ap}})$. We emphasize that throughout this study we always use the same aperture to compute both the total enclosed halo mass and the cluster observables; however, when studying a cylindrically-integrated observable, we shall still compare it to the spherically enclosed halo mass using the same numerical values for both r_{ap} and R_{ap} . The three main observables considered in this paper are $Y_{\text{SZ}}(< R_{\text{ap}})$, $M_{\text{gas}}(< r_{\text{ap}})$, and $T_{\text{mg}}(< r_{\text{ap}})$. Computing these quantities requires a model of the *thermal* pressure and gas density profiles, $P_{\text{th}}(r)$ and $\rho_{\text{gas}}(r)$, which we describe in Sections 2.2 and 2.3, respectively.

The self-similar model developed by Kaiser (1986) is a simple model of cluster evolution based on three assumptions: (i) clusters form from peaks in the initial density field of an Einstein–de Sitter universe with $\Omega_{\text{m}} = 1$, (ii) the amplitude of the primordial density fluctuations varies with spatial scale as a power law, and (iii) processes that impact cluster formation do not introduce additional physical scales to the problem (Kravtsov & Borgani 2012). Under these assumptions, the gravitational collapse of galaxy clusters is *self-similar*. However, various astrophysical processes, such

as turbulence, introduce additional physical scales, which result in cluster evolution that deviates from self-similarity. Before we investigate how non-thermal pressure support causes deviations from self-similarity, we briefly describe how the relevant observables (i.e., M_{gas} , T_{mg} , and Y_{SZ}) scale in the Kaiser (1986) model.

Given a particular overdensity definition, cluster mass and radius are interchangeable via $M_{\Delta} = (4\pi/3)\Delta\rho_{\text{x}}(z)r_{\Delta}^3$, where Δ is the overdensity factor. When haloes are defined with respect to a multiple of the critical density, $\rho_{\text{x}}(z) \equiv \rho_{\text{c}}(z) \propto E^2(z) = \Omega_{\text{m}}(1+z)^3 + \Omega_{\Lambda}$, whereas when they are defined with respect to the mean matter density, $\rho_{\text{x}}(z) \equiv \rho_{\text{m}}(z) \propto (1+z)^3$.

The Kaiser (1986) model assumes that the density profile of the gas, $\rho_{\text{gas}}(r)$, is self-similar and that its normalization is such that, for fixed r_{ap} , the ratio between the enclosed gas mass, given by

$$M_{\text{gas}}(< r_{\text{ap}}) = 4\pi \int_0^{r_{\text{ap}}} \rho_{\text{gas}}(r)r^2 dr, \quad (1)$$

and the enclosed total mass, $M(< r_{\text{ap}})$, is independent of halo mass. As we will see, the halo concentration-mass relation introduces an additional scale that causes the gas profile shapes to deviate from self-similarity. However, for large r_{ap} , the assumption of a fixed $M_{\text{gas}}(< r_{\text{ap}})/M(< r_{\text{ap}})$ is still reasonable because recent findings in both simulations and observations have found that the cumulative gas mass fraction approaches the cosmic baryon fraction at or below $\sim(1-2)r_{200m}$ (e.g., Kravtsov et al. 2005; Ettori et al. 2006; Planelles et al. 2013; Eckert et al. 2013; Mantz et al. 2014; Morandi et al. 2015) for clusters with $M_{500c} \geq 10^{14} h^{-1} M_{\odot}$ at $0 \leq z \leq 1$. This assumption is less realistic for lower mass haloes, where gas depletion due to feedback becomes significant.

The Kaiser (1986) model assumes that the gas is in HSE with the gravitational potential and that the logarithmic slopes of the gas density and thermal pressure profiles are independent of halo mass. Hence, from the HSE equation,

$$\frac{1}{\rho_{\text{gas}}(r)} \frac{dP(r)}{dr} = -\frac{d\Phi(r)}{dr} = \frac{GM(< r)}{r^2}, \quad (2)$$

where $P(r) = P_{\text{th}}(r)$ in the absence of non-thermal pressure, and assuming an ideal gas, we have that

$$M(< r) = -\frac{k_{\text{B}} T(r) r}{\mu m_{\text{p}} G} \left[\frac{d \ln T}{d \ln r} + \frac{d \ln \rho_{\text{gas}}}{d \ln r} \right], \quad (3)$$

where μm_{p} is the mean particle mass. This equation can be used to solve for $T(r)$ given $M(< r)$ and $\rho_{\text{gas}}(r)$, from which we compute the spherically-integrated gas mass-weighted temperature

$$T_{\text{mg}}(< r_{\text{ap}}) = \frac{4\pi}{M_{\text{gas}}(< r_{\text{ap}})} \int_0^{r_{\text{ap}}} \rho_{\text{gas}}(r) T(r) r^2 dr. \quad (4)$$

For the self-similar gas density profile assumed in the Kaiser (1986) model, this yields the following scaling relation

$$T_{\text{mg}}(< r_{\text{ap}}) \propto M(< r_{\text{ap}})^{2/3} [\Delta\rho_{\text{x}}(z)]^{1/3}. \quad (5)$$

Note the dependence on $\Delta\rho_{\text{x}}(z)$, which introduces a redshift dependence in the normalization of this scaling relation between cluster temperature and mass.

Lastly, to compute the cylindrically-integrated SZ signal, $Y_{\text{SZ}}(< R_{\text{ap}})$, we first calculate the Compton- y parameter by integrating the thermal pressure of the gas along the line-of-sight using

$$y_{\text{SZ}}(R) = 2 \int_R^{r_{\text{b}}} n_{\text{e}}(r) \frac{k_{\text{B}} T_{\text{e}}(r)}{m_{\text{e}} c^2} \sigma_{\text{T}} \frac{r dr}{\sqrt{r^2 - R^2}}, \quad (6)$$

where k_{B} , m_{e} , c , and σ_{T} are standard constants and $n_{\text{e}}(r)$ and $T_{\text{e}}(r)$

¹ Note that r_{500c} is the radius inside of which the mean density is equal to 500 times the *critical* density $\rho_{\text{c}}(z)$, whereas within r_{200m} , the mean density is 200 times the *mean matter* density, $\rho_{\text{m}}(z)$. For cluster mass scales, the virial radius $r_{\text{vir}} \approx 2r_{500c} \approx 0.8r_{200m}$ at $z = 0$.

denote the electron gas number density and temperature profiles. The line-of-sight integration is performed out to $r_b \equiv 2r_{200m}$, which is roughly consistent with the radius of the accretion shock beyond which the pressure profile rapidly drops to the ambient pressure of the intergalactic medium (see e.g., [Molnar et al. 2009](#); [Lau et al. 2015](#)). We then integrate $Y_{SZ}(R)$ over the aperture using

$$Y_{SZ}(< R_{ap}) = 2\pi \int_0^{R_{ap}} Y_{SZ}(R) R dR. \quad (7)$$

As can be seen from equation (6), the SZ signal is proportional to the product of the gas density and temperature. Hence, the self-similar [Kaiser \(1986\)](#) model predicts that

$$Y_{SZ}(< R_{ap}) \propto M_{gas}(< r_{ap}) T_{mg}(< r_{ap}) \propto M(< r_{ap})^{5/3} [\Delta\rho_x(z)]^{1/3}. \quad (8)$$

In Section 3.3, we study the deviations of these observable-mass relations from self-similarity due to the injection of turbulence via mass assembly. Note that of M_{gas} , T_{mg} , and Y_{SZ} , only Y_{SZ} is computed as a two-dimensional projected quantity in this work — hence, our T_{mg} and M_{gas} are not direct observables, but studying these spherically-integrated quantities is still illuminating with regards to understanding the $Y_{SZ} - M$ relation.

2.2 Total pressure and gas density profiles

We assume that the dark matter distribution of clusters follow the Navarro-Frenk-White (NFW) density profile ([Navarro et al. 1997](#)) with enclosed mass

$$M(< r) = M_{vir} \frac{f(c_{vir}r/r_{vir})}{f(c_{vir})}, \quad (9)$$

where M_{vir} , r_{vir} , and c_{vir} are the halo virial mass, radius, and concentration,² respectively, and $f(x) = \ln(1+x) - x/(1+x)$. Under this assumption, [Komatsu & Seljak \(2001, hereafter KS01\)](#) develop a polytropic gas model for clusters in HSE where the thermal pressure $P_{th}(r) \propto \rho_{gas}(r)T(r) \propto \rho_{gas}(r)^\Gamma$, with Γ the polytropic index.

However, by studying simulated galaxy clusters, [Shaw et al. \(2010\)](#) find that a polytropic model describes the *total* pressure profile $P_{tot}(r)$ better than $P_{th}(r)$. Hence, we use the model of [KS01](#) to compute $P_{tot}(r) \propto \rho_{gas}(r)T_{eff}(r) \propto \rho_{gas}(r)^\Gamma$. Here, $T_{eff}(r)$ is an effective temperature profile that accounts for both the thermal and non-thermal pressure, which we write as $T_{eff}(r) \equiv T_{eff,0}\theta(r)$. The resulting total pressure and gas density are thus parametrized as

$$P_{tot}(r) = P_0\theta(r)^{\frac{\Gamma}{\Gamma-1}} \quad \text{and} \quad \rho_{gas}(r) = \rho_0\theta(r)^{\frac{1}{\Gamma-1}}, \quad (10)$$

where all of P_0 , ρ_0 , and $\theta(r)$ depend on M_{vir} and c_{vir} .³ In addition, for reasons explained below, we have that $\Gamma = \Gamma(c_{vir})$. Plugging these parameterizations into the HSE equation (equation [2]), where we now use $P(r) = P_{tot}(r)$, yields

$$\theta(r, M_{vir}, c_{vir}) = 1 + \frac{\Gamma-1}{\Gamma} \frac{\rho_0}{P_0} [\Phi(0) - \Phi(r)], \quad (11)$$

² M_{vir} is the mass enclosed within r_{vir} , inside of which the mean density is equal to $\Delta_{vir}(z)$ times the critical density. At $z = 0$, $\Delta_{vir}(z) \approx 100$, and is otherwise well-described by [Bryan & Norman \(1998\)](#) for general z and cosmology. The concentration $c_{vir} = r_{vir}/r_s$, with r_s the NFW scale radius.

³ The native mass definition of the [KS01](#) gas model and our MAH models (Section 2.4) is that of $\Delta_{vir}(z)$. We convert between mass and radius definitions using the concentration model in equation (15) and adopt the ‘200m’ and ‘500c’ mass conventions for comparisons with various simulation and observational results.

with $\Phi(r)$ the NFW gravitational potential profile, given by

$$\Phi(r) = -\frac{GM_{vir}}{r_{vir}} \frac{c_{vir}}{f(c_{vir})} \frac{\ln(1 + c_{vir}r/r_{vir})}{c_{vir}r/r_{vir}}. \quad (12)$$

The two free parameters of the model, Γ and $P_0/\rho_0 \propto T_{eff,0}$ are determined by demanding that the gas density profile traces the dark matter density profile in the outer regions of the halo. Since the shape of the dark matter density profile depends on halo mass via the mass-concentration relation, both Γ and P_0/ρ_0 also depend on c_{vir} . We follow [KS01](#), adopting their polynomial fitting functions given by their equations (25) and (26).

Motivated by the discussion of $M_{gas}(< r_{ap})/M(< r_{ap})$ in Section 2.1, we set the normalization of $\rho_{gas}(r)$ such that $M_{gas}(< 2r_{200m})$ is equal to the cosmic baryon fraction Ω_b/Ω_m times $M(< 2r_{200m})$; our results are insensitive to the exact radius used to set this normalization.

2.3 Non-thermal pressure profile

In order to calculate cluster observables, we need to disentangle $P_{th}(r)$ from $P_{tot}(r) = P_{th}(r) + P_{nth}(r)$, where $P_{nth}(r)$ is the non-thermal pressure. We determine the non-thermal pressure by following the analytical model of [Shi & Komatsu \(2014, hereafter SK14\)](#). From the [KS01](#) total pressure and gas density profiles, we calculate the total velocity dispersion of the gas (per degree of freedom) $\sigma_{tot}^2(r, M_{vir}, c_{vir}) = P_{tot}(r)/\rho_{gas}(r) = (P_0/\rho_0)\theta(r)$. We emphasize that σ_{tot}^2 evolves in time due to changing mass *and* concentration. The ansatz of [SK14](#) is that the turbulent energy (per unit mass per degree of freedom) $\sigma_{nth}^2(r)$ dissipates on a time-scale proportional to the eddy turn-over time of the largest eddies, which is in turn proportional to the local orbital time $t_{dis}(r) = \beta t_{orb}(r)/2$, and a fraction η of the total energy injected into the cluster via mass growth is converted into turbulence. Based on this ansatz, the non-thermal energy evolves as

$$\frac{d\sigma_{nth}^2}{dt} = -\frac{\sigma_{nth}^2}{t_{dis}} + \eta \frac{d\sigma_{tot}^2}{dt}. \quad (13)$$

The free parameters are calibrated against cosmological simulations in [Shi et al. \(2015\)](#) to $\beta = 1$ and $\eta = 0.7$, which we adopt throughout. Determining σ_{nth}^2 at redshift z is an initial value problem; [SK14](#) find that the results are insensitive to the initial redshift z_i and initial σ_{nth}^2 . Hence, we use $z_i = 30$ and $\sigma_{nth}^2(r, z_i) = \eta\sigma_{tot}^2(r, z_i)$.⁴ With this sufficiently high initial redshift, the time between z_i and z is many multiples of the initial $t_{dis}(r)$ (i.e., $15 - 10^4$ times) for all r and z of interest, eliminating the impact of the initial value of σ_{nth}^2 . Note that σ_{nth}^2 is evolved independently for each cluster-centric radius r .

The fiducial timestep used in the σ_{nth}^2 evolution corresponds to 10% of the instantaneous cluster free-fall time at a critical overdensity of 200. At each timestep, the halo mass and concentration are updated based on the MAH model described below in Section 2.4. The updated $M_{vir}(z_j)$ and $c_{vir}(z_j)$ result in updated $\Gamma(c_{vir})$, $(P_0/\rho_0)(c_{vir})$, and $\Phi(r, M_{vir}, c_{vir})$, which we can use to compute $\sigma_{tot}^2(r, z_j)$. We then compute

$$\frac{d\sigma_{tot}^2}{dt}(r, z_j) = \frac{\sigma_{tot}^2(r, z_j) - \sigma_{tot}^2(r, z_{j-1})}{t(z_j) - t(z_{j-1})}, \quad (14)$$

⁴ We also impose the physical constraint that whenever $\sigma_{nth}^2(r, t_{j-1}) < -d\sigma_{nth}^2(r, t_{j-1})$, then $\sigma_{nth}^2(r, t_j) = 0$ rather than becoming negative; this can happen occasionally near the halo center, where t_{dis} is small.

after which we can compute $d\sigma_{\text{nth}}^2/dt$ to get our updated $\sigma_{\text{nth}}^2(r, z_j)$. Note that different $M_{\text{vir}}(z)$ and $c_{\text{vir}}(z)$ trajectories thus result in different $(d\sigma_{\text{tot}}^2/dt)(r, z)$ trajectories. Hence, for fixed M_{vir} at observation redshift z , all variance in the σ_{nth}^2 profiles is due to inter-cluster differences in MAHs.

With $\sigma_{\text{nth}}^2(r)$ computed, we define the non-thermal energy fraction as $f_{\text{nth}}(r) = \sigma_{\text{nth}}^2(r)/\sigma_{\text{tot}}^2(r)$. The thermal pressure profile is then $P_{\text{th}}(r) = [1 - f_{\text{nth}}(r)]P_{\text{tot}}(r)$.⁵ From $P_{\text{th}}(r)$ and $\rho_{\text{gas}}(r)$, we can compute the aforementioned cluster observables. In addition, we explore the mass and redshift dependence of the non-thermal pressure fraction and its implications for the HSE mass bias in Sections 3.1 and 3.2, respectively.

2.4 Mass accretion histories

The evolution of σ_{nth}^2 depends on the MAH of the cluster, $M_{\text{vir}}(z)$, the time derivative of which is encoded in $d\sigma_{\text{tot}}^2/dt$ (see equation (14) and preceding paragraph). Here, $M_{\text{vir}}(z)$ tracks the mass assembly history of the *main branch*, which is the branch of the halo merger tree that follows the main progenitor of the main progenitor of the main progenitor and so on (halo merger trees are discussed in detail in Section 2.1 of Jiang & van den Bosch 2016). We compute *individual* MAHs using the merger tree method described in Parkinson et al. (2008), a Monte Carlo approach based on the extended Press–Schechter (EPS; Bond et al. 1991) formalism, which the method comparison project of Jiang & van den Bosch (2014) finds to perform the best at reproducing merger trees in simulations. The Parkinson et al. (2008) method generates merger trees based on the ‘binary method with accretion’ of Cole et al. (2000) alongside a progenitor mass function modified from EPS theory to reproduce the merger statistics of the *Millenium Simulation* (Springel et al. 2005). See Section 2.2 of van den Bosch et al. (2014) for additional details regarding the specific implementation of the method. These Monte Carlo MAHs are used in our analysis of the observable-mass relations in Sections 3.3 and 3.4. When we are interested in the *average* properties of a given halo of mass $M_{\text{vir},0}$ at redshift of observation z_0 , we use the ‘universal model’ of the average MAH described in van den Bosch et al. (2014) (see their Section 4.1 and Appendix C). The average MAHs are used to study the properties of $f_{\text{nth}}(r)$ and the HSE bias in Sections 3.1 and 3.2.

For illustrative purposes, in Fig. 1, we show many different Monte Carlo-generated $M_{\text{vir}}(z)$ trajectories for haloes with $\log(M_{\text{vir}}(z=0)/[h^{-1}M_{\odot}]) = 14$. In addition, we overplot the average MAH predicted by the van den Bosch et al. (2014) model for a halo of the same mass, demonstrating good agreement.

Concentrations are determined using the model of Zhao et al. (2009) as modified by van den Bosch et al. (2014) to accurately reproduce the concentrations seen in *Bolshoi*. The halo concentrations are given by

$$c_{\text{vir}}(M_{\text{vir}}, t) = 4.0 \left[1 + \left(\frac{t}{3.40t_{0.04}} \right)^{6.5} \right]^{1/8}, \quad (15)$$

where $t_{0.04}$ is the proper time at which the halo’s progenitor has accumulated 4% of its mass M_{vir} at proper time t , which can be computed directly from the MAH. We have verified that the main results of this work are insensitive to the specific $c_{\text{vir}}(M_{\text{vir}}, z)$ model

⁵ Note that the temperature is related to the effective temperature (Section 2.2) via $T(r) = [1 - f_{\text{nth}}(r)]T_{\text{eff}}(r)$.

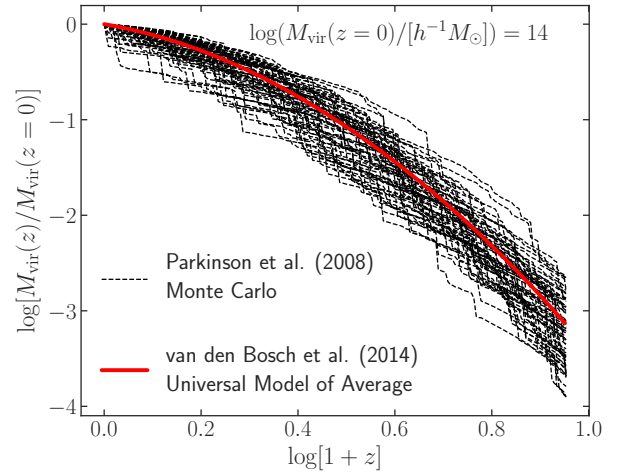


Figure 1. Example mass accretion histories, $M_{\text{vir}}(z)$, for haloes with a final mass of $\log(M_{\text{vir}}(z=0)/[h^{-1}M_{\odot}]) = 14$. The black, dashed lines correspond to individual MAHs generated by the Monte Carlo method of Parkinson et al. (2008) whereas the thick, red line represents the ‘universal model’ of the average MAH developed in van den Bosch et al. (2014). The individual MAHs are essential for studying the scatter in the observable-mass scaling relations (Sections 3.3 and 3.4), whereas the average MAH is used for studying properties of the non-thermal pressure fractions and HSE mass bias (Sections 3.1 and 3.2).

used (we isolate the effect of the $c_{\text{vir}}(M_{\text{vir}}, z)$ relation on our results in Section 3.3).

When discussing the effect of the mass assembly history on deviations from the self-similar observable-mass relations, it is convenient to use a summary statistic of $M_{\text{vir}}(z)$ that captures the mass accretion rate (MAR) over a finite period of time. Throughout, we use the definition of the MAR introduced in Diemer (2017), which encapsulates the change in $M_{200\text{m}}$ over one dynamical (or crossing) time, $t_{\text{dyn}} = 2r_{200\text{m}}/v_{200\text{m}}$, where $v_{200\text{m}}$ is the circular velocity at $r_{200\text{m}}$. This MAR is written as

$$\Gamma_{\text{dyn},200\text{m}} = \frac{\log[M_{200\text{m}}(a_{\text{obs}})] - \log[M_{200\text{m}}(a_1)]}{\log(a_{\text{obs}}) - \log(a_1)}, \quad (16)$$

where $a_{\text{obs}} = (1+z)^{-1}$ corresponds to the redshift of observation z and $a_1 = a(t_{\text{obs}} - t_{\text{dyn}})$ is the scale factor one dynamical time prior to observation.

All results have been tested for convergence with respect to (i) the temporal resolution of the MAH and associated σ_{nth}^2 equation integration, (ii) the spatial resolution of the cluster profiles used to integrate the observables, and, where relevant, (iii) the number of MC-generated MAH realizations used to compute observable-mass relationships.

2.5 Quantifying scaling relations

In our analysis of cluster scaling relations, we study individual, Monte Carlo-generated halo MAHs using the merger tree method of Parkinson et al. (2008). For each redshift of observation and cosmology considered, we generate 10,000 MAHs for haloes sampled uniformly in the mass range $12 \leq \log(M_{\text{vir}}(z)/[h^{-1}M_{\odot}]) \leq 15.5$. For consistency with other studies, the analysis in the main text uses the mass range of $14 \leq \log(M_{200\text{m}}/[h^{-1}M_{\odot}]) \leq 15.6$ (a total of $\sim 4,500$ clusters), but we use the lower-mass clusters to explore the effect of the mass cutoff on the relations in Appendix B. In

the latter, more-restricted mass regime, our assumption of a mass-independent $M_{\text{gas}}(< r_{\text{ap}})/M(< r_{\text{ap}})$ ratio is well-justified (see the discussion in Sections 2.1 and 2.2). For each MAH, the $f_{\text{nth}}(r)$ profile is evolved to the redshift of observation. Then, spanning a range of apertures, r_{ap} , we compute the observables, $M_{\text{gas}}(< r_{\text{ap}})$, $T_{\text{mg}}(< r_{\text{ap}})$, and $Y_{\text{SZ}}(< R_{\text{ap}})$, and the corresponding halo mass, $M(< r_{\text{ap}})$. We aim to elucidate how the slope, normalization, and scatter of the observable-mass relationships evolve with redshift and depend on aperture and cosmology. *Note that we use the same aperture to calculate both the observable and the enclosed mass.* It is sometimes the case in observational studies that the mass is measured within one aperture (e.g., r_{500c}) and the observable is measured within a larger aperture (e.g., $Y_{\text{SZ}}[< 5R_{500c}]$), which can introduce additional effects due to the mass-concentration relation. We emphasize that in the limit that $f_{\text{nth}} = 0$, the observables are computed purely from the KS01 model with $P_{\text{th}} = P_{\text{tot}}$, yielding the self-similar cluster scaling relations discussed in Section 2.1 with no scatter or deviation aside from that due to the mass-concentration relationship; thus, all scatter is due to the variance in the halo MAHs and its impact on the f_{nth} profile and halo concentrations. In particular, increased f_{nth} will result in T_{mg} and Y_{SZ} decreasing and falling below the self-similar curve.

For each observable $X_{\text{obs}}(< r_{\text{ap}})$, we compute the best-fit power-law relationship

$$X_{\text{obs}}(< r_{\text{ap}}) = 10^{\alpha} \left(\frac{M(< r_{\text{ap}})}{[10^{14} h^{-1} M_{\odot}]} \right)^{\beta}, \quad (17)$$

with α the normalization and β the power-law slope. We then compute the logarithmic residuals as

$$\mathcal{R} = \log(X_{\text{obs,fit}}) - \log(X_{\text{obs,true}}), \quad (18)$$

where $X_{\text{obs,fit}}$ is computed from equation (17) given the $M(< r_{\text{ap}})$ of each halo.⁶

We find that the log-residuals for the $T_{\text{mg}} - M$ and $Y_{\text{SZ}} - M$ relations are *not* normally distributed due to a strong right-skew (i.e., there is a long tail towards large \mathcal{R}). As we illustrate in Section 3.4, this is directly due to a right-skew in the recent MARS of the haloes and a correlation between $\Gamma_{\text{dyn},200m}$ and non-thermal pressure support, which ultimately suppresses Y_{SZ} . As shown in Fig. 2, the mean of and variance in $\Gamma_{\text{dyn},200m}$ grows with both halo mass and redshift for MAHs generated via the Parkinson et al. (2008) method; this is directly responsible for a variety of trends in Section 3. Note that part of the strong right-skew is due to the fact that the MAR is bounded from below by zero, but is not bounded from above. A deviation from normality (and log-normality) of the residual distribution of $Y_{\text{SZ}} - M$ in the form of a right-skew is also seen, albeit to a milder degree, in the non-radiative (NR) hydrodynamically-simulated clusters of Battaglia et al. (2012) (see their Fig. 22 and note their reversed definition of residual), indicating that in the absence of additional sources of non-thermal pressure beyond that introduced due to the halo assembly history, the residual distribution does indeed reflect the distribution of halo MARS. However, with the addition of radiative cooling, star formation, supernovae feedback, and AGN feedback, Battaglia et al. (2012) find that the residual distribution of $Y_{\text{SZ}} - M$ approaches normality (*not* log-normality). The relationship between the MAR and the $Y_{\text{SZ}} - M$ residuals will be discussed in more detail in Section 3.4.

⁶ Note that our residual definition is opposite in sign to that which is normally used in the literature. As we show in Section 3.4, \mathcal{R} as defined in equation (18) correlates with the halo MAR.

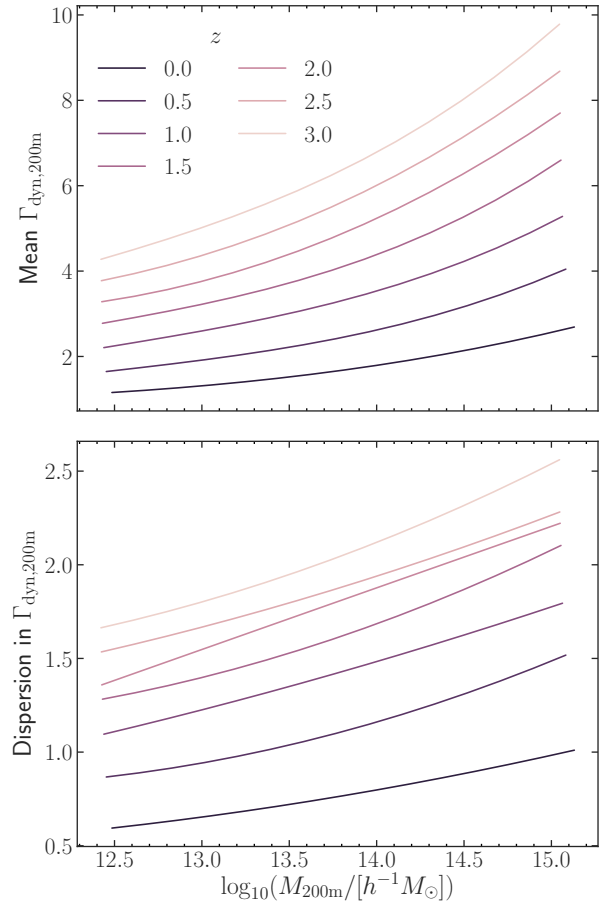


Figure 2. The mean of and dispersion in halo MARS, $\Gamma_{\text{dyn},200m}$ (defined in equation [16]), as a function of halo mass and redshift for halo MAHs generated via the Parkinson et al. (2008) method. The $\Gamma_{\text{dyn},200m}$ distribution is skewed (most strongly at low M_{200m} and z); hence, “dispersion” is defined as half of the 16 – 84 percentile range. Note that both the mean of and dispersion in $\Gamma_{\text{dyn},200m}$ grow with M_{200m} and z . These trends are ultimately responsible for the same trends seen in the non-thermal pressure fractions (Section 3.1) and for the increased scatter and decreased normalization in the scaling relations as z increases (Section 3.3).

The correlation between $\Gamma_{\text{dyn},200m}$ and non-thermal pressure support also causes the scatter in the scaling relations to increase systematically with halo mass (the implications of this with respect to survey mass cuts is discussed in Appendix B). Regardless of the log-residual distribution’s deviation from normality and heteroscedasticity, ordinary least squares remains the best linear unbiased estimator of the mass-observable regression coefficients (Plackett 1950). These details, however, do affect how we should report the scatter seen in the observable-mass relations. Typically, in analysis of both simulated and observed clusters, the residual distribution is assumed to be log-normal with mean zero. Under this assumption, one can simply report the scatter as the standard deviation of the log-residuals in dex, $\sigma_{\mathcal{R}}$. Due to the substantial deviation from log-normality in our case and in an effort to make comparisons to results in the literature, we report scatter in dex instead based on half of the 16 – 84 percentile range of \mathcal{R} . In either case, scatter in dex can be converted to the mean fractional/percent scatter using $\sigma_{\Delta X}/X \approx \sigma_{\mathcal{R}} \ln(10)$, which is accurate to $\lesssim 4\%$ for $\sigma_{\mathcal{R}} \leq 0.1$ dex. Some confusion in the literature has arisen due to this dex-to-percent scatter conversion; hence, for pedagogical

purposes, we derive the relationship between $\sigma_{\mathcal{R}}$ and $\sigma_{\Delta X}/X$ in Appendix A. Our reported percent scatters are smaller by roughly 1% (in absolute units, not relative) than they would be if we instead used the standard deviation of the log-residuals. Lastly, we emphasize that a skewed residual distribution should be checked for in observational analyses and must be taken into account when reporting scatter in the observable-mass relations and when using such relations to place constraints on cosmological parameters; the scatter may be overestimated if one assumes log-normality when instead the residual distribution is substantially skewed.

3 RESULTS

We start this section off by exploring the non-thermal pressure fraction profiles of the average cluster observed with a given mass at a particular redshift (Section 3.1). We then study the resulting average HSE mass bias introduced due to non-thermal pressure support (and its dependence on halo mass and redshift) in Section 3.2. We proceed to calculate the scaling relations of samples of individual clusters, studying their dependence on aperture radius, cosmology, redshift, and halo mass limit in Section 3.3. Lastly, we identify a strong correlation between the halo MAR and the $Y_{\text{SZ}} - M$ residual in Section 3.4, briefly discussing the potential utility of such a relationship.

3.1 Non-thermal pressure fractions

Since the cornerstone of our analysis is the SK14 model of the non-thermal pressure, we first study its predicted $f_{\text{nth}}(r)$ profiles for an average cluster of mass $M_{200\text{m}}$ observed at z using the ‘universal model’ of the MAH from van den Bosch et al. (2014). In Fig. 3, we plot the $f_{\text{nth}}(r)$ profiles for clusters of several different masses as a function of $r/r_{200\text{m}}$. The choice of $r_{200\text{m}}$ is motivated by Nelson et al. (2014b), who find that the $f_{\text{nth}}(r/r_{200\text{m}})$ profiles of their sample of NR hydrodynamically-simulated galaxy clusters is universal throughout their time evolution (this will be discussed more below); this universality is absent when normalized by $r_{200\text{c}}$.

In the left panels of Fig. 3, we hold $M_{200\text{m}}$ fixed and show how the f_{nth} radial profile changes with observation redshift. As halo mass increases, the non-thermal pressure fraction increases. This can be explained by the fact that higher mass haloes assemble at later times (e.g., Lacey & Cole 1993; van den Bosch 2002; Li et al. 2008); hence, their recent MAR will be higher than that of lower mass haloes (cf. Fig. 2). More non-thermal energy has been recently injected into a system with a higher recent MAR, which results in a larger f_{nth} . We also see that at fixed halo mass, f_{nth} is larger for clusters observed at higher redshift. This can be explained similarly to the previous point: in order for a halo to obtain a mass M by $z_1 > z_2$, it must have accreted mass more rapidly than a halo with mass M at z_2 (cf. Fig. 2). Note that the fraction of non-thermal pressure is substantial, especially in the cluster outskirts — f_{nth} surpasses 50% by around $\sim r_{200\text{m}}$ for high-mass haloes and haloes at large z .

We now explore the dependence of $f_{\text{nth}}(r/r_{200\text{m}})$ on peak height, $\nu_{200\text{m}} = \delta_{\text{c}}(z)/\sigma(M_{200\text{m}})$.⁷ In the right panels of Fig. 3,

Parameter	Value
<i>A</i>	0.495
<i>B</i>	0.719
<i>C</i>	1.417
<i>D</i>	−0.166
<i>E</i>	0.265
<i>F</i>	−2.116

Table 1. Calibrated parameters for the $f_{\text{nth}}(r/r_{200\text{m}}, \nu_{200\text{m}})$ fitting function described by equation (19), which reproduces the model non-thermal pressure fractions to roughly 10% accuracy in the radial range of $0.2 \leq r/r_{200\text{m}} \leq 2.0$ at $z = 1$. Note that there is only a weak redshift dependence in the model predictions, as can be seen in Fig. 3, so this fitting function can be easily used to make rough predictions regardless of redshift.

we hold $\nu_{200\text{m}}$ fixed to several different values and show how $f_{\text{nth}}(r/r_{200\text{m}})$ evolves with redshift in each case (i.e., $M_{200\text{m}}$ is varied with z such that $\nu_{200\text{m}}$ remains constant). As is apparent, there is far less redshift evolution at fixed peak height than at fixed mass. We overplot the fitting function of Nelson et al. (2014b) for their universal $f_{\text{nth}}(r/r_{200\text{m}})$ profile, finding that for the peak height consistent with the $z = 0$ cluster masses studied in their work ($\nu_{200\text{m}} \approx 4$), the predictions of the SK14 model agree well with what is seen in the simulations. There is an exception to this agreement, however, in the central regions of the clusters, where the model underpredicts the non-thermal pressure fraction compared to that seen in the Nelson et al. (2014b) simulations. As discussed in Shi et al. (2015), this is likely due to (i) the model’s assumption of a one-to-one relationship between the cluster radius and the turbulence dissipation timescale (note that this assumption is the primary source of the f_{nth} radial dependence) and (ii) the potential need to incorporate radius and redshift dependence into η to properly model the relative importance of high-Mach accretion shocks and low-Mach internal shocks.

The model does not predict a universal $f_{\text{nth}}(r/r_{200\text{m}})$ profile, which clearly has a dependence on $\nu_{200\text{m}}$ that, to good approximation, accounts for the dependence on both $M_{200\text{m}}$ and z . At first, this appears to be at odds with the simulated clusters studied in Nelson et al. (2014b). However, they studied the evolution of a cluster sample through *time*, with $M_{200\text{m}}$ only spanning half an order of magnitude in the range $14.8 < \log(M_{200\text{m}}/[h^{-1}M_{\odot}]) < 15.4$ at $z = 0$. This detail, combined with their use of a z -dependent mass cutoff for the cluster sample, likely resulted in the Nelson et al. (2014b) sample spanning an insufficient range in $\nu_{200\text{m}}$ to isolate evolution in redshift from universality in $f_{\text{nth}}(r/r_{200\text{m}})$ at fixed $\nu_{200\text{m}}$.

Motivated by our finding that, to good approximation, $f_{\text{nth}} = f_{\text{nth}}(r/r_{200\text{m}}|\nu_{200\text{m}})$, we present a fitting function for the non-thermal pressure fraction that includes this $\nu_{200\text{m}}$ dependence:

$$f_{\text{nth}}(\tilde{r}|\nu) = 1 - \left[A \left(1 + e^{-(\tilde{r}/B)^C} \right) \left(\frac{\nu}{4.1} \right)^{\frac{D}{(1+(\tilde{r}/E)^F)}} \right]. \quad (19)$$

Here, $\nu = \nu_{200\text{m}}$ and $\tilde{r} = r/r_{200\text{m}}$. The parameters of this function are calibrated to match the $z = 1$ predictions of the model across $1.0 \leq \nu_{200\text{m}} \leq 4.2$ and are listed in Table 1. The fit, shown as dotted curves in Fig. 3, is accurate to roughly 10% over the radial range of $0.2 \leq r/r_{200\text{m}} \leq 2.0$.

3.2 Hydrostatic mass bias

As discussed in the introduction, cluster mass inferences based on X-ray and SZ observations are typically made under the assumption of HSE between the observed thermal pressure profile and the grav-

⁷ Here, $\delta_{\text{c}}(z) = \delta_{\text{c}}(z = 0)/D_+(z)$ is the critical overdensity for collapse (Gunn & Gott 1972), $D_+(z)$ is the linear growth factor normalized to unity at $z = 0$, and $\sigma(M_{200\text{m}})$ is the rms mass fluctuation in a Lagrangian volume corresponding to $M_{200\text{m}}$.

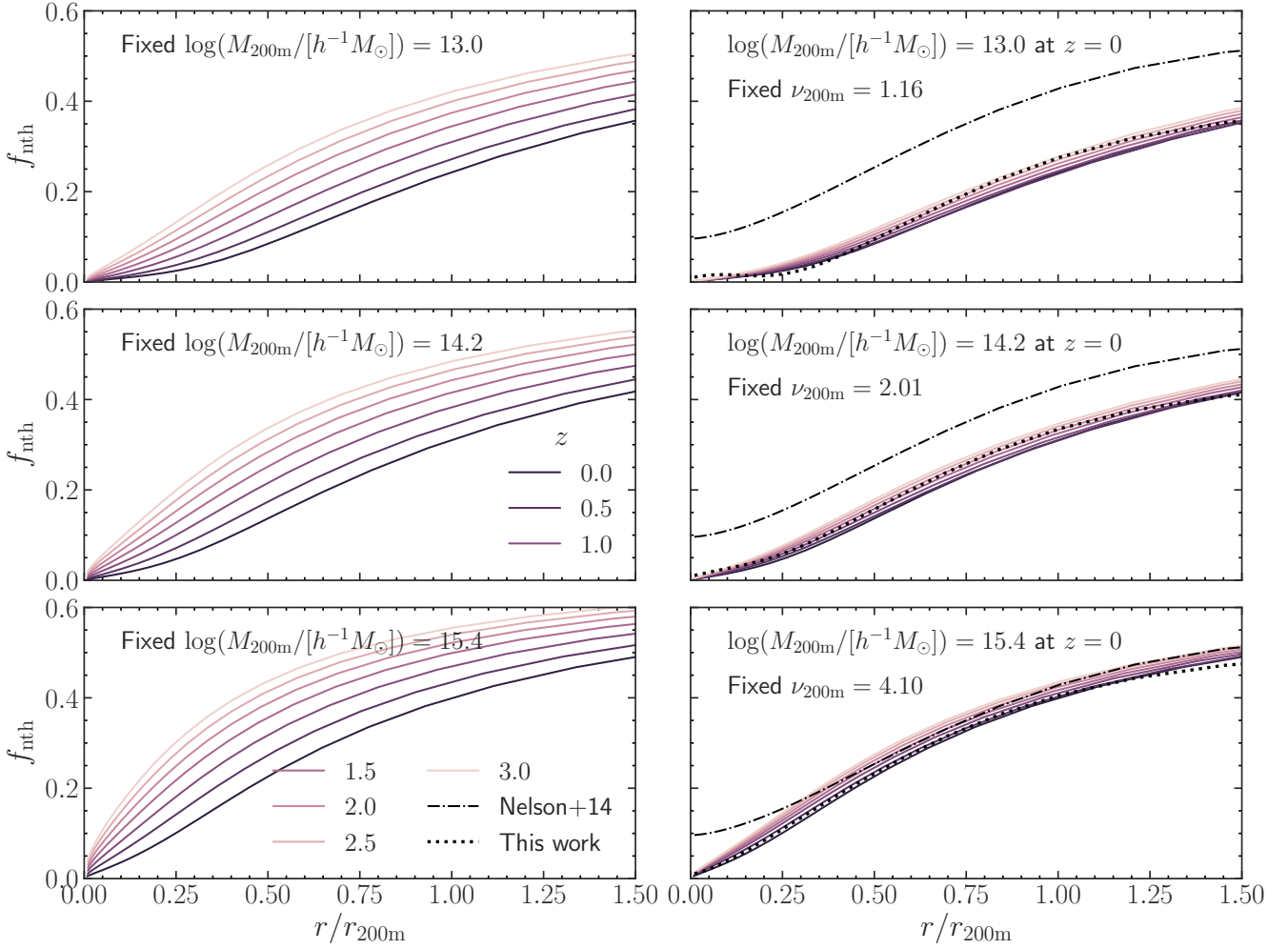


Figure 3. The non-thermal pressure fraction profiles of clusters $f_{\text{nth}}(r/r_{200\text{m}})$ as predicted by the SK14 model combined with the ‘universal model’ of the MAH from van den Bosch et al. (2014). (left) Each panel holds the cluster mass $M_{200\text{m}}$ fixed and varies the redshift of observation. As either $M_{200\text{m}}$ or z increases, the non-thermal pressure fraction increases due to the increased recent mass accretion rate. (right) Each panel holds the peak height $\nu_{200\text{m}}$ fixed such that the $z = 0$ mass is the same as that in the corresponding left panel. There is minimal redshift evolution in $f_{\text{nth}}(r/r_{200\text{m}})$ at fixed peak height. The ‘universal profile’ seen in the simulated clusters of Nelson et al. (2014b) is over-plotted (dot-dashed line), illustrating the peak height-dependence that was not seen in their cluster sample due to their limited $z = 0$ mass range. Our fitting function described by equation (19) and Table 1 (dotted line) incorporates $\nu_{200\text{m}}$ -dependence and reproduces the SK14 model at $z = 1$ at roughly 10% accuracy in the radial range of $0.2 \leq r/r_{200\text{m}} \leq 2.0$.

itational potential. The true cluster mass, however, is related to the *total* pressure profile, and thus any unaccounted-for sources of non-thermal pressure result in underprediction of the cluster mass. The f_{nth} profiles predicted by the SK14 model can be used to estimate the corresponding HSE mass bias.

From the HSE equation (i.e., equation [2]), one can compute how much the true mass M is underpredicted (M^{HSE}) as a function of mass and redshift. Assuming an accurate determination of the gas density and thermal pressure profiles, which can be made possible through the combination of X-ray and SZ observations (e.g., Ameglio et al. 2009; Eckert et al. 2019; Ettori et al. 2019), this underprediction is written as

$$\frac{M^{\text{HSE}}(< r)}{M(< r)} = \frac{dP_{\text{th}}/dr}{dP_{\text{tot}}/dr} = [1 - f_{\text{nth}}(r)] - P_{\text{tot}}(r) \frac{df_{\text{nth}}/dr}{dP_{\text{tot}}/dr}. \quad (20)$$

Since dP_{tot}/dr is negative and df_{nth}/dr is positive, this ratio should always be larger than $1 - f_{\text{nth}}(r)$ for measurements of mass enclosed

within r . Note that this estimate of the HSE bias neglects potential effects due to the deviation from spherical symmetry and projection effects. In Fig. 4, we plot the predictions for $M_{500\text{c}}^{\text{HSE}}/M_{500\text{c}}$ as a function of $M_{500\text{c}}$ and redshift of observation. We use $r_{\text{ap}} = r_{500\text{c}}$ ($\approx 0.4r_{200\text{m}}$) since this is the aperture most commonly used for X-ray-based cluster mass estimation. At this radius, the SK14 model is in good agreement with the f_{nth} profiles of the simulated clusters of Nelson et al. (2014b), which only include NR hydrodynamics. Hence, additional sources of non-thermal pressure due to magnetic fields, cosmic rays, supernova feedback, among others, are not included and thus, we expect these estimates of the magnitude of the HSE bias to be *lower bounds*. The SK14 model predicts that the magnitude of the HSE bias increases considerably with cluster mass and observation redshift. At $z = 0$, HSE-based masses underestimate the true masses by less than 10% even for the highest mass clusters. However, at $z \sim 2 - 3$, the HSE bias results in substantial

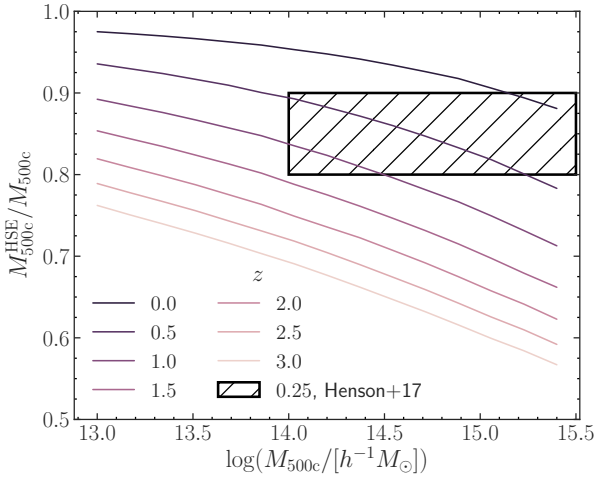


Figure 4. The HSE mass bias for M_{500c} , computed using equation (20), as predicted using the SK14 model of the non-thermal pressure. The “bias” increases as M_{500c}^{HSE}/M_{500c} decreases. These results are roughly consistent with the simulated clusters studied in Henson et al. (2017, at $z = 0.25$, hatched black box), although our results can be considered lower bounds, as sources of non-thermal pressure in addition to those due to mass assembly are not modeled and will increase the bias. The mass bias increases substantially with redshift, motivating further simulation studies focused on the HSE bias redshift evolution.

underprediction of the true mass, by roughly 20% at group scales and as much as 30 – 40% for high-mass clusters.

In the $z = 0.25$ simulated cluster sample from the BAHAMAS (McCarthy et al. 2017) and MACSIS (Barnes et al. 2017a) hydrodynamic simulations studied in Henson et al. (2017), which include star formation, radiative cooling, and feedback from supernovae and AGN (hereafter referred to as “full-physics” simulations), the HSE bias found is $M_{500c}^{HSE}/M_{500c} \approx 0.8 - 0.9$ in the mass range $14 \leq \log(M_{500c}/[h^{-1}M_{\odot}]) \leq 15.5$. Their bias is only marginally larger than that predicted by our model (Fig. 4), which is most likely due to the additional sources of non-thermal pressure captured in the full-physics simulations. Similarly, Ansarifard et al. (2019) reports a median of $M_{500c}^{HSE}/M_{500c} \approx 0.9$ for simulated clusters at $z = 0$ in a similar mass range. On the other hand, using synthetic X-ray observations, Barnes et al. (2020) report biases as significant as $M_{500c}^{HSE}/M_{500c} \approx 0.7$ for simulated clusters at $z = 0.1$ with $\log(M_{500c}/M_{\odot}) \approx 15.3$ — they find that this is primarily due to the use of a single temperature fit to the full cluster spectrum. For reference, a larger bias is necessary ($M_{500c}^{HSE}/M_{500c} \approx 0.6$) in order to resolve the tension between cosmological parameter estimates based on the cluster mass function and cosmic microwave background approaches (Salvati et al. 2019).

We emphasize that these calculations are based on the average MAH for a cluster observed with a given mass and redshift. Clusters that are more disturbed (i.e., have a higher recent MAR) will generally have larger biases than the average, as their non-thermal pressure fraction will be larger. In fact, the difference between the HSE bias of an individual cluster and the average (at fixed halo mass and redshift) should correlate with the MAR; as we discuss in Section 3.4, a strong correlation also arises between the residuals of the $Y_{SZ} - M$ relation and the MAR. To date, we are not aware of any simulation studies that characterize the evolution of the HSE bias over a reasonably large range of redshifts. Based on the results of Fig. 4, such a study is warranted, as the redshift dependence of the

HSE bias predicted will be important to account for in cluster count analyses that include high- z cluster samples from future surveys.

3.3 Cluster scaling relations

Having demonstrated that the average f_{nth} profiles (and resultant HSE biases) predicted by the SK14 model are in good agreement with predictions from hydrodynamical simulations, we proceed to use the model to study the cluster scaling relationships. In Fig. 5, we plot the best fit normalization, slope, and percent scatter for the $z = 0$ relations as a function of r_{ap} . In order to provide insight into the model predictions and disentangle the nonlinear interactions between its various components, we calculate the cluster observables in three different ways. First, we compute cluster observables using the “full model” described in Sections 2.2 and 2.3. We then repeat the calculations while holding the halo concentrations fixed to $c_{vir} = 5$ (referred to as the “fixed c_{vir} model”), isolating the impact of the mass-concentration relation. Going further, we perform a third set of calculations: while continuing to hold c_{vir} fixed, we now also replace the radius-dependent turbulence dissipation timescale with its value at r_{200m} (i.e., $t_{dis}(r) = t_{dis}(r_{200m})$); referred to as the “fixed c_{vir} and t_{dis} model”). This elucidates the impact of the radial dependence of $t_{dis}(r)$. Note that in this final case, the f_{nth} profile is nearly constant with radius for a given halo and all variation in f_{nth} between haloes is due to variation in MAHs.

3.3.1 $M_{gas} - M$ relation

Beginning with the $M_{gas} - M$ relation (middle column of Fig. 5), our model predicts no scatter in the absence of a MAH-dependence on the concentration. This is simply due to our use of the KS01 model for ρ_{gas} , which has no dependence on the halo MAH or f_{nth} but only on c_{vir} . In the full model, the scatter goes to zero and the slope goes to unity as $r_{ap} \rightarrow 2r_{200m}$; this is simply due to our chosen gas density normalization that $M_{gas}(< 2r_{200m}) = (\Omega_b/\Omega_m)M(< 2r_{200m})$. The effect of the mass-concentration relation and its intrinsic scatter on the shape of both the dark matter and gas density profiles is responsible for the small change in slope (and increase in scatter) of $M_{gas} - M$ as aperture radius decreases (see e.g., Fujita & Aung 2019). Even with fixed concentrations, the difference between the gas and dark matter density profile shapes is responsible for a slight dependence on r_{ap} in the $M_{gas} - M$ normalization.

3.3.2 $T_{mg} - M$ relation

Next, we direct our attention to the mass-weighted temperature, T_{mg} (left-hand column of Fig. 5). In the fixed c_{vir} and t_{dis} model, the scatter and slope are independent of aperture. More-massive clusters have larger MAR, which drives larger f_{nth} (see the left panels of Fig. 3). For f_{nth} independent of radius, we have that $T_{mg} \propto (1 - f_{nth})$, which, combined with the fact that f_{nth} grows with halo mass, results in the slope of $T_{mg} - M$ lying below that of self-similarity. In this simplified model, the aperture-independent scatter in $T_{mg} - M$ is also driven solely by variation in halo MAHs and is most sensitive to the mass evolution over the previous dynamical time. Moving on to the fixed c_{vir} model, we notice that incorporation of a radius-dependent $t_{dis}(r)$ introduces a dependence on aperture into the slope and scatter of $T_{mg} - M$. Higher mass clusters tend to have $f_{nth}(r)$ profiles that are overall larger in magnitude and grow more rapidly with radius (most notably in the inner radii; see once again the left panels of Fig. 3). Hence, their temperature profiles will be

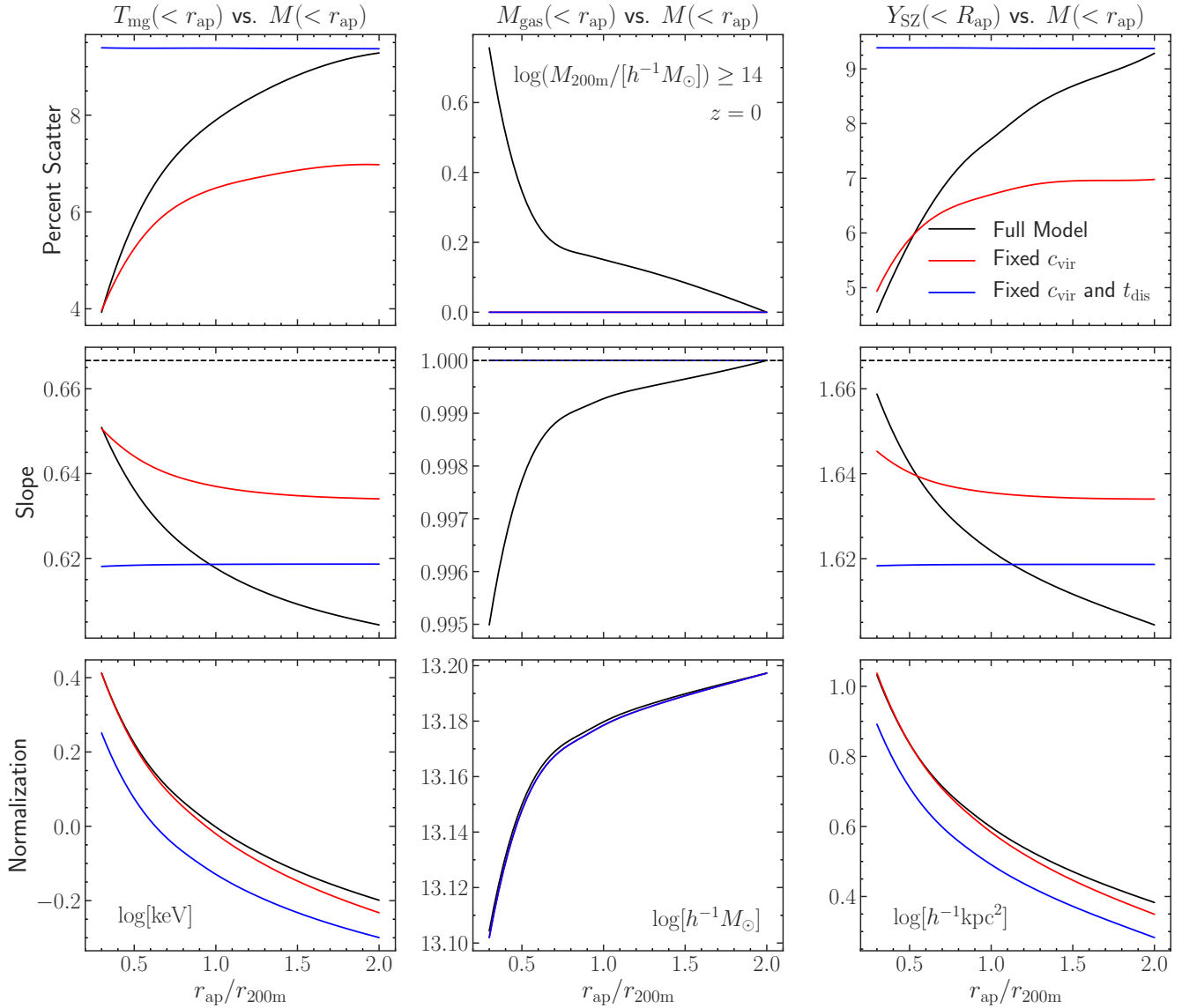


Figure 5. The best fit normalization, slope, and percent scatter of the $z = 0$ observable-mass relations, described by equation (17) for $T_{\text{mg}}(< r_{\text{ap}}) - M(< r_{\text{ap}})$, $M_{\text{gas}}(< r_{\text{ap}}) - M(< r_{\text{ap}})$, and $Y_{\text{SZ}}(< R_{\text{ap}}) - M(< r_{\text{ap}})$. The fit parameters are shown as a function of the aperture radius, r_{ap} , in units of $r_{200\text{m}}$; note that the same aperture is used to compute both the observable and the total mass. In these fits, $\sim 4,500$ clusters in the mass range $14 \leq \log(M_{200\text{m}}/[h^{-1}M_{\odot}]) \leq 15.6$ are used; the effect of varying the lower mass cutoff is discussed and illustrated in Appendix B. The black dashed lines indicate the slopes predicted by the self-similar relations. The observables are computed using the “full model” described in Sections 2.2 and 2.3 (black curves) as well as two simplified models, one of which holds $c_{\text{vir}} = 5$ fixed (red curves) in order to isolate the effects of the mass-concentration relation and another that holds both $c_{\text{vir}} = 5$ fixed and replaces the radius-dependent turbulence dissipation timescale with its value at $r_{200\text{m}}$ (blue curves), isolating the interaction between r_{ap} and the radius-dependence of $f_{\text{nth}}(r)$. See the main text in Section 3.3 for detailed explanations of the trends with r_{ap} .

more suppressed overall relative to self-similarity. In addition, since $df_{\text{nth}}(r)/dr$ increases with halo mass (in the inner radii), the slope of $T_{\text{mg}} - M$ decreases further from self-similarity as r_{ap} increases. The scatter in $f_{\text{nth}}(r)$ grows with radius due to the radially increasing $t_{\text{dis}}(r)$; because of this, the scatter in $T_{\text{mg}} - M$ grows with aperture radius. Lastly, by looking at the full model, we see two effects due to the mass-concentration relation. First, $c_{\text{vir}}(M, z)$ results in further reduction in the $T_{\text{mg}} - M$ slope away from self-similarity. Additionally, the variance in $c_{\text{vir}}(M, z)$ propagates to additional scatter in $T_{\text{mg}} - M$ that becomes more substantial as r_{ap} increases. Finally, the normalization of the $T_{\text{mg}} - M$ relation decreases with increasing

aperture for a simple reason. Since the cluster temperature decreases with radius, the mass-weighted temperature must decrease as the aperture radius increases. In addition, the pivot mass used for the relations is $M(< r_{\text{ap}}) = 10^{14} h^{-1} M_{\odot}$ regardless of aperture. Hence, this pivot mass at larger r_{ap} corresponds to a smaller total (virial) mass and thus a lower temperature normalization.

3.3.3 $Y_{\text{SZ}} - M$ relation

Lastly, we turn to the integrated SZ signal, Y_{SZ} (right-hand column of Fig. 5). Since Y_{SZ} is simply the cylindrically-integrated pressure

profile, to good approximation $Y_{\text{SZ}} \propto M_{\text{gas}} T_{\text{mg}}$. This relationship bares out straightforwardly in Fig. 5, as the slope of the $Y_{\text{SZ}} - M$ relation evolves roughly as the sum of the slopes of the $T_{\text{mg}} - M$ and $M_{\text{gas}} - M$ relations. In our calculations, the only source of scatter in $M_{\text{gas}} - M$ is the mass-concentration relation. However, as described above, the variance in the cluster MAHs drives the scatter in $T_{\text{mg}} - M$ and increases considerably with aperture. Thus, the scatter in the $Y_{\text{SZ}} - M$ relation is driven by the scatter in the $T_{\text{mg}} - M$ relation. Regarding the reduction in normalization and slope of $Y_{\text{SZ}} - M$ with increasing aperture, we find similar trends to those reported in Nagai (2006).

3.3.4 Redshift evolution

Having explored the non-linear interactions between aperture radius, halo concentration, and turbulence dissipation timescales in our model, we move on to study the redshift evolution of $Y_{\text{SZ}} - M$. In Fig. 6, we plot the best fit normalization, slope, and percent scatter for the $Y_{\text{SZ}} - M$ scaling relation as a function of r_{ap} for different samples of clusters observed at $0 \leq z \leq 3$. When using a spherical overdensity definition relative to the mean matter density (such as $r_{200\text{m}}$), the full self-similar scaling relation is $Y_{\text{SZ}} \propto M^{5/3}(1+z) = [M(1+z)^{3/5}]^{5/3}$ (see Section 2.1). Thus, scaling the masses by $(1+z)^{3/5}$ accounts for the redshift evolution predicted by the self-similar model. Any additional redshift evolution in the normalization or slope of $Y_{\text{SZ}} - M(1+z)^{3/5}$ indicates z -dependent deviations from self-similarity. The model predicts some rich trends with observation redshift. The normalization of $Y_{\text{SZ}} - M(1+z)^{3/5}$ decreases slightly with increasing z , with the decrease being larger when a larger r_{ap} is used. This is simply due to the fact that at earlier times, halo MARS were generally higher (see Fig. 2), resulting in an overall increase in non-thermal pressure support due to turbulence, and thus suppression in Y_{SZ} , with increasing z (as in Fig. 3). For $r_{\text{ap}} \lesssim r_{200\text{m}}$, the slope of the relation decreases with increasing z . This is due to the fact that f_{nth} in the inner regions increases more strongly with z in more massive haloes (this can be seen in the left panels of Fig. 3). The apparent trend-reversal at larger aperture radii is caused by the mass-concentration relation and its redshift evolution. The model also predicts that scatter in $Y_{\text{SZ}} - M$ increases with z , which is directly a consequence of the increased variance in halo MARS at earlier times (see Fig. 2).

These redshift evolution trends are in overall agreement with predictions from NR hydrodynamical simulations, most clearly with regards to the scatter evolution. The studies by Battaglia et al. (2012), Le Brun et al. (2017), and Planelles et al. (2017) all find that the scatter in $Y_{\text{SZ}} - M$ increases slightly with increasing z in their NR simulations (although only for high-mass clusters in the case of Le Brun et al. 2017). On the other hand, only Battaglia et al. (2012) finds that the $Y_{\text{SZ}} - M$ slope tends to decrease slightly away from self-similarity with z , whereas Le Brun et al. (2017) and Planelles et al. (2017) find minimal redshift evolution in the slope. The $Y_{\text{SZ}} - M$ slope increases when going to the full-physics AGN simulations slightly in Battaglia et al. (2012) and significantly (up to ~ 2) in Le Brun et al. (2017), whereas it remains virtually unchanged in Planelles et al. (2017), highlighting a point of tension between simulation results. These studies (as well as Nagai 2006) have reported that the redshift evolution of the normalization shows no significant deviation from self-similarity when $r_{\text{ap}} = r_{500\text{c}}$, consistent with our findings for $r_{\text{ap}} \approx 0.4r_{200\text{m}}$. However, the predictions of Fig. 6 show that deviations from self-similarity are expected to increase in magnitude when larger aperture radii are employed. This, combined with the current tension between the results of various simulation studies

(particularly with regards to the dependence of the $Y_{\text{SZ}} - M$ slope on z and AGN physics), suggests that the redshift evolution (and its dependence on r_{ap}) of cluster scaling relations needs to be studied in more depth using large cluster counts. In particular, a comparison between NR and full-physics simulations will help determine whether or not the trends due to variance in MAHs predicted by our model are washed out by additional physical processes (such as AGN and supernova feedback, etc.). With upcoming surveys pushing to larger cluster counts and higher z , characterizing the redshift evolution of these scaling relations is of paramount importance. If our model prediction that scatter in the relations increases significantly with redshift is correct, then it will be important to continue to develop lower-scatter mass proxies with less sensitivity to redshift in order to maximally utilize upcoming high-redshift cluster data to their full potential for precision cosmology.

3.3.5 Dependence on cosmology

In Fig. 7, we consider the impact of single-parameter variations about the fiducial (Planck Collaboration et al. 2018) cosmology on $Y_{\text{SZ}} - M$ at $z = 0$. Over the range of cosmologies studied, we find small but systematic trends. Recently, Singh et al. (2019) studied the effect of variations in the cosmological parameters on X-ray-based cluster scaling relations using full-physics hydrodynamics simulations based on the *Magneticum* suite.⁸ Using an aperture of $r_{\text{ap}} = r_{\text{vir}}$, they find that the slope and normalization of $Y_{\text{SZ}} - M$ systematically decrease with increasing Ω_{m} . We qualitatively reproduce these trends. While the changes to the properties of the $Y_{\text{SZ}} - M$ relation due to large changes in the cosmological parameters (relative to the posterior distributions of the Planck Collaboration et al. 2018 parameters) are small, both the present work and Singh et al. (2019) illustrate that more accurate models of the cluster scaling relations (and their dependence on cosmology) may eventually provide an additional approach to constraining the cosmological parameters given large ($\sim 10^4 - 10^5$) cluster samples from next-generation missions, such as *eROSITA*, Simons Observatory, and CMB-S4. However, for such an approach to be feasible, future analytical gas models must account for additional significant physical processes (see Section 4) and the accuracy of their predictions must be validated against simulations that span a realistic range of cosmological parameters. In addition, we demonstrate in Appendix B that decreasing the halo mass cutoff used to compute the scaling relations results in changes to the slope and scatter that may be degenerate with changes due to cosmology.

3.3.6 Scatter comparison with simulations and observations

The simple model of SK14 demonstrates that a substantial fraction of the total scatter in the $Y_{\text{SZ}} - M$ relation is likely to arise from inter-cluster variance in the non-thermal pressure, which in turn arises from variance in the halo MAHs. There have been numerous studies that address the scatter in the $Y_{\text{SZ}} - M$ relation using simulations (da Silva et al. 2004; Nagai 2006; Battaglia et al. 2012; Kay et al. 2012; Sembolini et al. 2013; Pike et al. 2014; Yu et al. 2015; Hahn et al. 2017; Le Brun et al. 2017; Planelles et al. 2017; Henden et al. 2019; Singh et al. 2019) as well as observations using both weak-lensing and HSE X-ray masses (Bonamente et al. 2008; Hoekstra et al. 2012; Marrone et al. 2012; Planck Collaboration et al. 2014; Czakon et al. 2015; Sereno et al. 2015; Nagarajan et al.

⁸ <http://magneticum.org/>

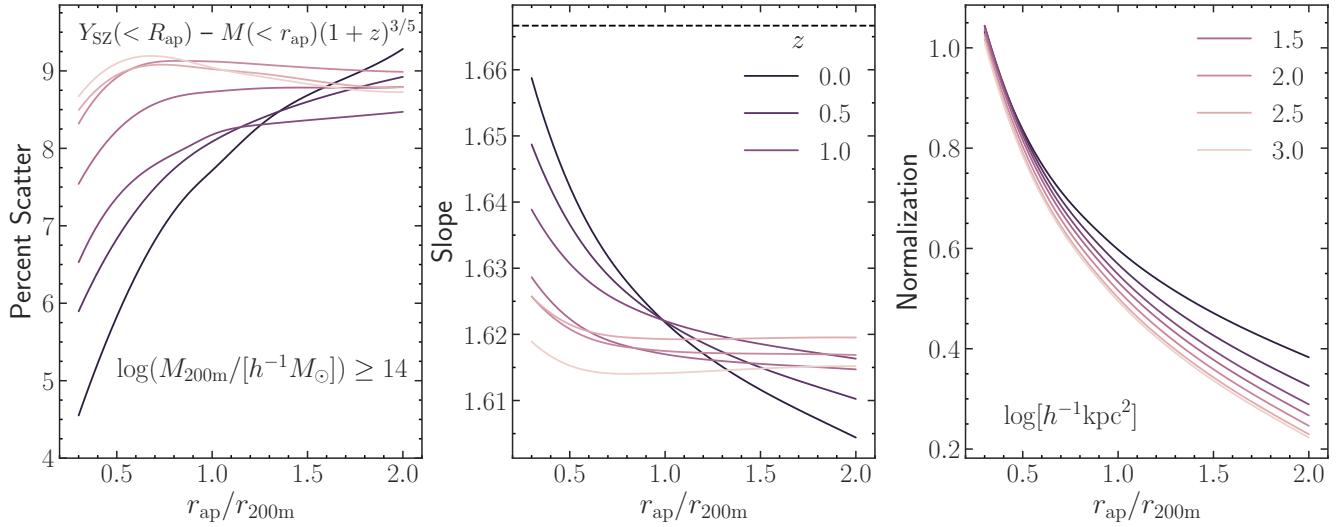


Figure 6. The best fit normalization, slope, and percent scatter of the $Y_{\text{SZ}}(< R_{\text{ap}}) - M(< r_{\text{ap}})$ relation, with masses scaled by the self-similarity evolution factor $(1+z)^{3/5}$. The fit parameters are shown as a function of r_{ap} and different curves illustrate the redshift evolution from $z = 0$ to $z = 3$. In these fits, $\sim 4,500$ clusters uniformly distributed in the mass range $14 \leq \log(M_{200\text{m}}(z)/[h^{-1}M_{\odot}]) \leq 15.6$ are used for each z . As observation redshift increases, the slope and normalization tend to decrease while the scatter increases. The interaction of the redshift-dependence of the mass-concentration relation is responsible for the apparent trend-reversals around $r_{\text{ap}} \approx r_{200\text{m}}$. Similar results have been seen in hydrodynamics simulations (e.g., Nagai 2006; Battaglia et al. 2012; Le Brun et al. 2017; Planelles et al. 2017).

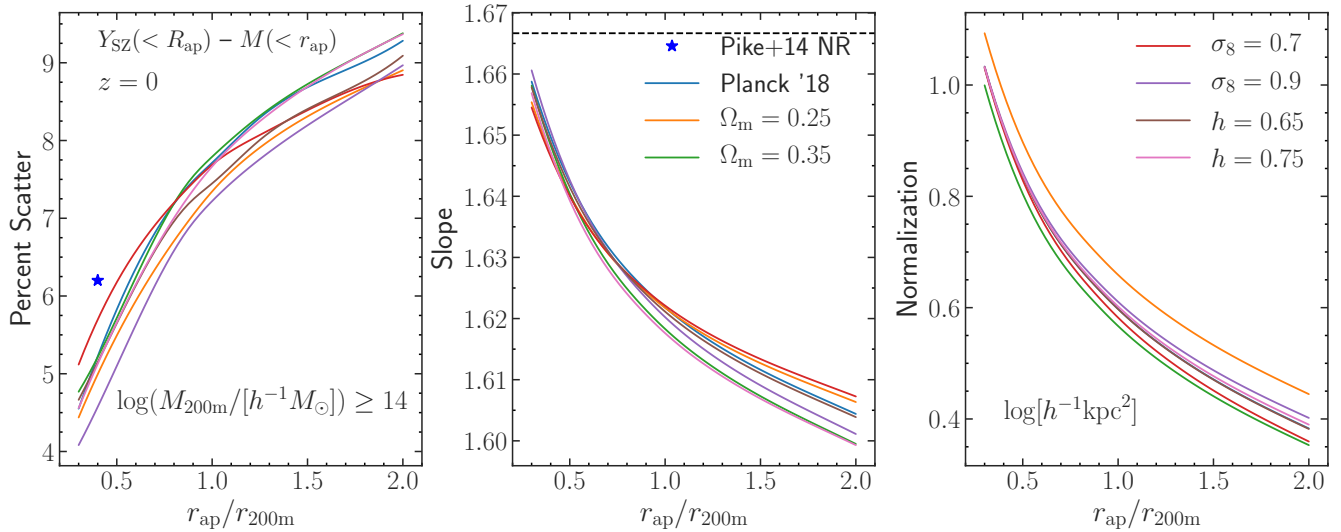


Figure 7. The best fit normalization, slope, and percent scatter of the $Y_{\text{SZ}}(< R_{\text{ap}}) - M(< r_{\text{ap}})$ scaling relation at $z = 0$. The fit parameters are shown as a function of the aperture radius, r_{ap} , in units of $r_{200\text{m}}$. In these fits, $\sim 4,500$ clusters in the mass range $14 \leq \log(M_{200\text{m}}/[h^{-1}M_{\odot}]) \leq 15.6$ are used. Each curve represents a different cosmology, varied about the fiducial Planck Collaboration et al. (2018) cosmological parameters — the variations in $Y_{\text{SZ}} - M$ with cosmology are subtle, but the trends we find are consistent with the simulations of Singh et al. (2019). Our predicted scatter in $Y_{\text{SZ}} - M$ for $r_{\text{ap}} = r_{500\text{c}} \approx 0.4r_{200\text{m}}$ (at $z = 0$) is only slightly below the scatter seen in the NR hydrodynamical simulations of Pike et al. (2014). The majority of simulation studies predict scatter in the range of 10 – 16%. Hence, much of the scatter in $Y_{\text{SZ}} - M$ is simply due to inter-cluster variation in the mass assembly histories, which drives variance in the cluster $f_{\text{th}}(r)$ profiles.

2019). At $z = 0$, most simulation studies find an intrinsic scatter in Y_{SZ} at fixed mass of 10 – 16% (roughly 0.04 – 0.07 dex) when using $R_{\text{ap}} = R_{500\text{c}} \approx 0.4r_{200\text{m}}$. There are indications in these studies that the scatter increases slightly when going from NR runs to full-physics simulations with AGN (see e.g., Battaglia et al. 2012). On the lower end, the $Y_{\text{SZ}}(< R_{500\text{c}}) - M(< r_{500\text{c}})$ relation computed

using the NR simulations of Pike et al. (2014) has a scatter of just 6%. For comparison, the intrinsic scatter in the $Y_{\text{SZ}} - M$ relation predicted by our model, using the same aperture (see Fig. 7) and with the same mass cutoff ($\log(M_{200\text{m}}/[h^{-1}M_{\odot}]) \geq 14$), is $\sim 5\%$. It is important to note that as SZ observation sensitivity increases, observable-mass scaling relations will be measured using larger

apertures, most notably $R_{\text{ap}} = 5R_{500c} \approx 2R_{200m}$. While our computation illustrates that with this larger aperture the assembly-driven scatter in $Y_{\text{SZ}} - M$ increases to 9%, it is possible that contributions to the intrinsic scatter from the cluster core (largely due to feedback) will be reduced. Hence, the optimal aperture radius that minimizes the intrinsic scatter in $Y_{\text{SZ}} - M$ is yet to be determined. Observational studies tend to find a higher intrinsic scatter in the wider range of 14 – 35% (0.06 – 0.15 dex), most of which use $R_{\text{ap}} = R_{500c}$, but similar results are found with $R_{\text{ap}} = R_{2500c}$. If a 5% (10%) Gaussian scatter is added to the cluster masses to mimic observational uncertainties, our predicted scatter in $Y_{\text{SZ}}(< R_{500c}) - M(< r_{500c})$ increases from $\sim 5\%$ to 10% (18%), which is more consistent with the observed results. The observational errors, particularly with regards to mass estimation, are still large; hence, the true intrinsic scatter in the relation is expected to be significantly lower than the values reported in the current observational literature, further motivating the development of more-accurate mass estimation techniques. However, it is also possible that additional processes not modeled in the full-physics simulations (e.g., magnetic fields and cosmic rays) are responsible for some of the additional intrinsic scatter observed.

3.4 Mass accretion rate prediction

As discussed in the Section 2.5, the model predicts a skewed distribution of the log-residuals of the $Y_{\text{SZ}} - M$ relation due to the skewed distribution of MARs, $\Gamma_{\text{dyn},200m}$ (see equation [16]). In the SK14 model, a high recent MAR will increase $f_{\text{nth}}(r)$, resulting in a decrease in the magnitude of the observables, T_{mg} and Y_{SZ} (at fixed halo mass). In Fig. 8, we plot the distributions of $\Gamma_{\text{dyn},200m}$ and the log-residuals, \mathcal{R} , computed for the $Y_{\text{SZ}}(< R_{200m}) - M(< r_{200m})$ relation at $z = 0$. There is a strong right-skew in the \mathcal{R} distribution towards over-predictions, and this right-skew is mirrored in the MAR distribution towards a small fraction of haloes with high $\Gamma_{\text{dyn},200m}$ (i.e., disturbed clusters). The skewness in \mathcal{R} is present regardless of mass cutoff or aperture employed.

The correspondence between the two distributions suggests that the $Y_{\text{SZ}} - M$ residual, which is itself an observable quantity, is likely to correlate with the underlying halo MAR. The ability to estimate $\Gamma_{\text{dyn},200m}$ from an observable would be powerful since, as discussed in Diemer et al. (2017), $\Gamma_{\text{dyn},200m}$ is closely connected to the splashback radius and mass, r_{sp}/r_{200m} and M_{sp}/M_{200m} . The splashback radius has been suggested as a better, physically-motivated definition for the halo boundary (Adhikari et al. 2014; Diemer & Kravtsov 2014; More et al. 2015; Mansfield et al. 2017; Xhakaj et al. 2019), but it has proven difficult thus far to observe r_{sp} for individual clusters.

In Fig. 9, we plot the cluster MARs against their $Y_{\text{SZ}} - M$ log-residuals for several different redshifts. Diemer et al. (2017) present a fitting function for the median MAR seen in cosmological simulations as a function of z and v_{200m} , which we denote $\Gamma_{\text{dyn},200m}^*$ and use to normalize our $\Gamma_{\text{dyn},200m}$ values. There is a strong trend between the scaling relation log-residual and the median-normalized MAR, with a Pearson $\rho = 0.68$ and Spearman $r_s = 0.73$. The slope of the relation tends to decrease slightly with z . Importantly, for $\mathcal{R} = 0$, the trend predicts that $\Gamma_{\text{dyn},200m}/\Gamma_{\text{dyn},200m}^* \approx 1$; in other words, if the cluster falls on the best-fit line for the $Y_{\text{SZ}} - M$ relation, its MAR tends to be around the median for a halo of its mass at z . It is unclear whether or not such a strong trend between the residuals and halo MAR exists in real clusters, since previous simulation studies (e.g., Battaglia et al. 2012) have found that the MAR-driven skewness in the $Y_{\text{SZ}} - M$ residuals decreases and the distribution

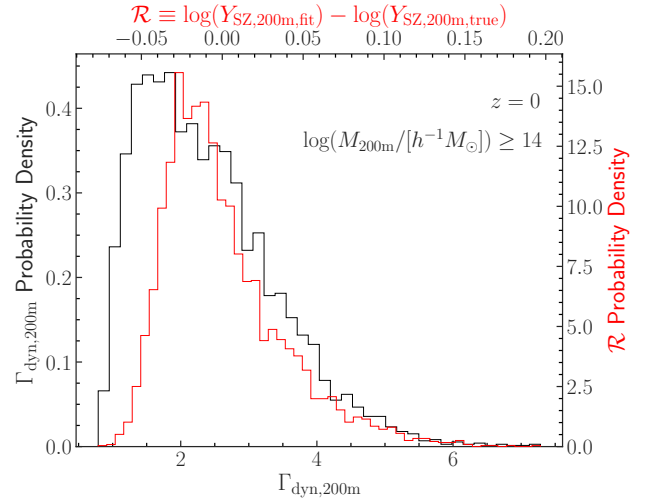


Figure 8. The distributions of halo MARs, $\Gamma_{\text{dyn},200m}$, defined by equation (16), and the log-residuals \mathcal{R} of the $Y_{\text{SZ}} - M$ relation. The scaling relation is computed at $z = 0$ for clusters in the mass range $14 \leq \log(M(r_{200m})/[h^{-1}M_{\odot}]) \leq 15.6$. The right-skew of the MAR distribution towards a minority of disturbed clusters is responsible for the right-skew in the \mathcal{R} distribution, as a high MAR increases f_{nth} and reduces the magnitude of the observables. The correspondence between the distributions suggests a correlation between the two quantities (see Fig. 9).

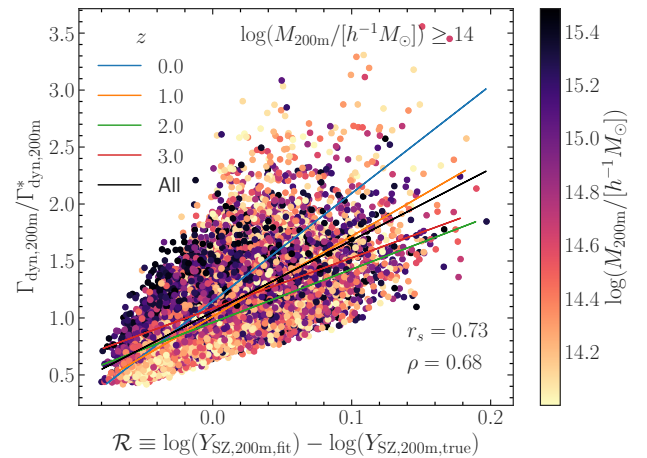


Figure 9. The relationship between the MARs and the $Y_{\text{SZ}} - M$ log-residuals for clusters at $0 \leq z \leq 3$ and in the mass range $\log(M_{200m}/[h^{-1}M_{\odot}]) \geq 14$. The MARs are normalized by the median MAR of haloes of a given z and v_{200m} using the fitting function of Diemer et al. (2017). At higher $\Gamma_{\text{dyn},200m}$, a halo tends to have more non-thermal pressure, which reduces the magnitude of Y_{SZ} , ultimately increasing \mathcal{R} . The trend is strong, with a Pearson $\rho = 0.68$ and Spearman $r_s = 0.73$ when including all redshifts. There is a slight trend in the slope with z , but the overall relation is roughly $\Gamma_{\text{dyn},200m}/\Gamma_{\text{dyn},200m}^* \approx 6\mathcal{R} + 1$. If present in full-physics simulations, this $\Gamma_{\text{dyn},200m} - \mathcal{R}$ relation may provide a link between the splashback radius and the observable residual, \mathcal{R} .

approaches normality when additional physics beyond NR hydrodynamics is modeled in the simulations. The relationship between the observable $Y_{\text{SZ}} - M$ log-residuals and $\Gamma_{\text{dyn},200m}$ should be explored in future full-physics simulation studies in order to quantitatively measure the strength of the $\Gamma_{\text{dyn},200m} - \mathcal{R}$ relation and forecast its predictive power for determining other secondary cluster properties

that have recently been tied to the MAR, such as assembly bias (Sunayama & More 2019) and the asphericity of the ICM (Chen et al. 2019).

4 DISCUSSION

Our approach assumes that non-thermal pressure is dominated by turbulence generated during mass assembly. The SK14 model of the non-thermal pressure profile does not yet take into account various secondary effects due to baryonic physics, many of which will likely increase the intrinsic scatter in the scaling relations from what is presented here, especially for low-mass haloes and when small apertures are used. Radiative cooling and star formation results in the condensation of gas into the center of the cluster, reducing the baryon budget. Both Shaw et al. (2010) and Flender et al. (2017) modeled this by assuming that the gas adiabatically contracts or expands due to the change in total gas mass. Feedback due to AGN and supernovae provide additional sources of turbulence, especially in the inner regions of the cluster (e.g., Vazza et al. 2013; Zhuravleva et al. 2014; Chadayammuri et al. 2020). These feedback effects become more significant as the halo mass decreases; hence, they must be accurately modeled in order to successfully quantify the thermodynamic properties of low-mass haloes through stacked measurements from upcoming microwave and X-ray surveys.

Substantial turbulent energy can also be injected into the cluster outskirts by the magneto-thermal instability (Parrish et al. 2012; McCourt et al. 2013). Additionally, observations of non-thermal X-ray emission and radio haloes (e.g., Million & Allen 2009; Kale et al. 2013) imply additional non-thermal pressure due to cosmic rays and magnetic fields. Strong constraints have been placed on the magnetic field strength in the ICM, limiting the magnetic field-associated pressure to be much smaller than the thermal pressure ($\approx 5\%$, Dolag & Schindler 2000; Iapichino & Brügggen 2012). Observations of γ -ray emission in nearby clusters provide constraints on the pressure due to cosmic ray protons generated from shocks in the ICM to be less than 2% of the thermal pressure (Ackermann et al. 2014; Shirasaki et al. 2019). Some simulations, however, suggest that cosmic rays could provide almost 50% of the total pressure in the cluster cores (Sijacki et al. 2008). Thus, although the overall additional non-thermal pressure due to magnetic fields and cosmic rays is likely small, better constraints are still warranted in order to determine the importance of incorporating their effects into future models of the total non-thermal pressure support.

Throughout our work, we assume spherically symmetric pressure and gas profiles for the clusters. The observational analysis of Arnaud et al. (2010) has shown that deviations from spherical symmetry and variations in cluster shapes can lead to scatter in the spherically-averaged pressure profiles. The recent hydrodynamical simulation study of Chen et al. (2019) has also reported that deviations from spherical symmetry increase the scatter in X-ray-based observable-mass scaling relations, additionally illustrating that the ellipticity of the ICM may be seeded by the MAH. Hence, the impact of mass assembly on the scatter in both SZ and X-ray observable-mass relations studied using our approach should still be regarded as a lower bound. The strength of future theoretical models will be greatly increased by incorporating the effect of mass accretion on triaxiality and cluster shape.

We have also neglected the impact of line-of-sight projection effects on the cluster observables. In particular, we study some spherically-integrated observables (i.e., M_{gas} and T_{mg}) and cut off the $y_{\text{SZ}}(R)$ line-of-sight integration at $2r_{200\text{m}}$. However, simulated light cone studies have demonstrated that a non-negligible fraction

of the SZ signal arises from the warm diffuse gas residing outside of groups and clusters (Hallman et al. 2007). Furthermore, Shirasaki et al. (2016) found that the projection of correlated structures along the line-of-sight introduces additional scatter into the scaling relation between the tSZ effect signal and the weak lensing mass. Thus, future gas models that aim to be combined with N -body simulations for efficient production of mock light cones must take into account the impact of the warm-hot intergalactic medium and other correlated structures along the line-of-sight.

5 CONCLUSION AND FUTURE OUTLOOK

We quantified the effects of mass assembly-driven turbulence on the $Y_{\text{SZ}} - M$ scaling relation. This was accomplished by combining a simple model of the total pressure and gas density profiles, a model of the evolution of non-thermal pressure, and Monte Carlo-generated halo mass accretion histories. We summarize our most salient findings below:

- The average non-thermal pressure fraction profiles $f_{\text{nth}}(r)$ tend to increase as halo mass or observation redshift increases. This is simply due to the fact that (i) higher mass haloes assemble later and (ii) a higher redshift of observation requires more rapid mass accretion at fixed halo mass.
- When radii are normalized by $r_{200\text{m}}$, the model predicts $f_{\text{nth}}(r/r_{200\text{m}})$ profiles that exhibit near-universality in redshift at fixed peak height $v_{200\text{m}}$. This finding is consistent with the simulation study of Nelson et al. (2014b). We provide a fitting function for $f_{\text{nth}}(r/r_{200\text{m}}|v_{200\text{m}})$ described by equation (19) and Table 1.
- As a consequence of $f_{\text{nth}}(r)$ increasing with halo mass and redshift, the model predicts that the magnitude of the average HSE mass bias (i.e., the deviation of the HSE-inferred mass from the true mass) also experiences these same trends.
- The scatter in the $Y_{\text{SZ}} - M$ relation due solely to inter-cluster variance in the halo MAHs ranges from 5 – 9%, increasing with aperture radius and z . Most NR hydrodynamical simulations predict 10 – 15% scatter. Thus, our model predicts that assembly-driven turbulence is responsible for a substantial fraction of the total scatter in $Y_{\text{SZ}} - M$.
- The slope of $Y_{\text{SZ}} - M$ tends to decrease slightly away from the self-similarity slope of 5/3 as aperture, redshift, or halo mass limit increases. This dependence on aperture was also reported in Nagai (2006).
- There are small trends in the slope, normalization, and scatter of $Y_{\text{SZ}} - M$ with cosmology. The trends seen in Fig. 7 are consistent with those seen in the X-ray observable-mass relations of the simulated clusters in Singh et al. (2019). The perturbations in $Y_{\text{SZ}} - M$ due to cosmology are similar in magnitude to those seen due to variations in the lower mass cutoff used for computing the relation. This indicates that careful control of sample selection will be essential for any attempt to use cluster scaling relations to constrain cosmological parameters.
- The model predicts a skewed distribution of log-residuals \mathcal{R} in $Y_{\text{SZ}} - M$ due to the skewed distribution of $\Gamma_{\text{dyn},200\text{m}}$, in agreement with the NR hydrodynamical simulations of Battaglia et al. (2012). We find that $\Gamma_{\text{dyn},200\text{m}}$ correlates tightly with \mathcal{R} (Spearman $r_s = 0.73$), potentially introducing a new observational approach to estimating the mass accretion rate via $Y_{\text{SZ}} - M$.

The non-thermal pressure support present in galaxy clusters must be taken into account in order to make accurate HSE mass estimates and utilize the full statistical power that will be available in next-generation X-ray and SZ surveys for cluster count-based cos-

mological analyses. By studying the non-thermal pressure fraction profile, which is an important component of analytical models of the ICM (Shaw et al. 2010; Flender et al. 2017), we highlighted the dependence of accretion-driven turbulence on halo mass and redshift. As survey sensitivity continues to grow, the need to model and correct for the HSE mass bias over a wide range of halo masses and redshifts (especially smaller group mass haloes and high-redshift systems) is becoming increasingly important. This work represents a step towards developing a more accurate analytical model of the hot gas in groups and clusters, which will help (i) disentangle the effects of AGN/supernovae feedback from the non-thermal pressure driven by the structure formation process and (ii) model the cosmological dependence of the ICM. A promising next step in model development should involve incorporating the effects of galaxy formation physics into the dark matter and gas density models (e.g., Schneider et al. 2019), which would enable the modeling of both galaxy formation and structure formation physics in a unified analytical framework. Such a step (as well as modeling other processes discussed in Section 4) will be crucial for combining the ICM model with models of the galaxy-halo connection and N -body simulations to generate a physically motivated and computationally efficient framework for interpreting forthcoming multi-wavelength cosmological datasets, ultimately enabling the use of correlation statistics from multi-wavelength cosmological surveys to constrain cosmology and astrophysics (Shirasaki et al. 2020).

Currently, the best observations of bulk and turbulent motions in the ICM are of the Perseus cluster core, where the *Hitomi* X-ray observatory has reported high-resolution measurements of emission line Doppler shifting and broadening (Hitomi Collaboration et al. 2018; Simionescu et al. 2019b, for a recent review). In the near future, *XRISM/Resolve* (Tashiro et al. 2018) and *Athena/X-IFU* (Barret et al. 2016) will measure the turbulence in the ICM for many nearby clusters and within the cores of more distant clusters, providing an opportunity to check the $f_{\text{nth}}(r)$ model, correct for the HSE mass bias, and properly calibrate the mass scale (Ota et al. 2018). Furthermore, the *Lynx* X-ray Surveyor (Gaskin et al. 2019) and *Cosmic Web Explorer* (Simionescu et al. 2019a) have been proposed as future-generation X-ray telescopes that would enable exquisite measurements of turbulence out to the halo outskirts of an unprecedentedly large sample down to the galaxy mass scale.

In the future, millimetre-wave observations may provide a promising and complementary lens into the thermodynamics and gas motions in the ICM via the thermal and kinematic SZ effects (see e.g., Mroczkowski et al. 2019). Upcoming and proposed microwave instruments, such as the TolTEC camera,⁹ CCAT-prime,¹⁰ CMB-HD (Sehgal et al. 2019), and Voyage2050 (Basu et al. 2019), will enable high-resolution SZ spectral imaging of clusters. This additional spectral information encodes a measurement of the kinematic SZ effect, which can be used to separate the cluster peculiar velocity and internal velocity dispersion (Inogamov & Sunyaev 2003; Nagai et al. 2003; Sayers et al. 2019), thus providing a direct measurement of the non-thermal pressure support. Furthermore, since the strength of the SZ signal is independent of redshift, this approach can be used to observe the redshift-dependence of $f_{\text{nth}}(r)$. Lastly, these observations will facilitate relativistic SZ corrections, which can be leveraged to study temperature structures in the ICM and mitigate the biases in the derived SZ and X-ray temperatures (see e.g., Chluba et al. 2012, 2013; Lee et al. 2019).

Finally, previous attempts at measuring the mass accretion rate of clusters via its relationship to the splashback radius have suffered from systematic uncertainties such as selection and projection effects (Baxter et al. 2017; Busch & White 2017; Zu et al. 2017). The strong correlation between $\Gamma_{\text{dyn},200\text{m}}$ and the log-residuals \mathcal{R} of the $Y_{SZ} - M$ relation highlighted in this study may provide an alternative means to measure the MAR, provided that the relationship is not washed out by other sources of non-thermal pressure or by observational errors. In addition to this $\Gamma_{\text{dyn},200\text{m}} - \mathcal{R}$ relation, machine learning algorithms may provide an alternative approach that enables more accurate determinations of both $\Gamma_{\text{dyn},200\text{m}}$ and the cluster mass, employing input features such as images of the ICM and summary statistics that quantify the cluster shape (e.g., Green et al. 2019; Ntampaka et al. 2019).

ACKNOWLEDGEMENTS

SBG is supported by the US National Science Foundation Graduate Research Fellowship under Grant No. DGE-1752134. DN acknowledges support by National Science Foundation grant AST-1412768 and the hospitality at the Aspen Center for Physics, which is supported by National Science Foundation grant PHY-1607611. FCvdB is supported by the National Aeronautics and Space Administration through Grant Nos. 17-ATP17-0028 and 19-ATP19-0059 issued as part of the Astrophysics Theory Program and received additional support from the Klaus Tschira foundation. This work was supported in part by the facilities and staff of the Yale Center for Research Computing.

REFERENCES

- Abazajian K., et al., 2019, arXiv e-prints, p. arXiv:1907.04473
 Ackermann M., et al., 2014, *ApJ*, **787**, 18
 Ade P., et al., 2019, *J. Cosmology Astropart. Phys.*, **2019**, 056
 Adhikari S., Dalal N., Chamberlain R. T., 2014, *J. Cosmology Astropart. Phys.*, **2014**, 019
 Allen S. W., Evrard A. E., Mantz A. B., 2011, *ARA&A*, **49**, 409
 Ameglio S., Borgani S., Pierpaoli E., Dolag K., Ettori S., Morandi A., 2009, *MNRAS*, **394**, 479
 Ansarifard S., et al., 2019, arXiv e-prints, p. arXiv:1911.07878
 Applegate D. E., et al., 2014, *MNRAS*, **439**, 48
 Applegate D. E., et al., 2016, *MNRAS*, **457**, 1522
 Arnaud M., Pratt G. W., Piffaretti R., Böhringer H., Croston J. H., Pointecouteau E., 2010, *A&A*, **517**, A92
 Avestruz C., Nagai D., Lau E. T., 2016, *ApJ*, **833**, 227
 Barnes D. J., Kay S. T., Henson M. A., McCarthy I. G., Schaye J., Jenkins A., 2017a, *MNRAS*, **465**, 213
 Barnes D. J., et al., 2017b, *MNRAS*, **471**, 1088
 Barnes D. J., Vogelsberger M., Pearce F. A., Pop A.-R., Kannan R., Cao K., Kay S. T., Hernquist L., 2020, arXiv e-prints, p. arXiv:2001.11508
 Barret D., et al., 2016, in Proc. SPIE, p. 99052F, doi:10.1117/12.2232432
 Basu K., et al., 2019, arXiv e-prints, p. arXiv:1909.01592
 Battaglia N., Bond J. R., Pfrommer C., Sievers J. L., Sijacki D., 2010, *ApJ*, **725**, 91
 Battaglia N., Bond J. R., Pfrommer C., Sievers J. L., 2012, *ApJ*, **758**, 74
 Battaglia N., Hill J. C., Murray N., 2015, *ApJ*, **812**, 154
 Baxter E., et al., 2017, *ApJ*, **841**, 18
 Biffi V., et al., 2016, *ApJ*, **827**, 112
 Bolliet B., Comis B., Komatsu E., Macías-Pérez J. F., 2018, *MNRAS*, **477**, 4957
 Bonamente M., Joy M., LaRoque S. J., Carlstrom J. E., Nagai D., Marrone D. P., 2008, *ApJ*, **675**, 106
 Bond J. R., Cole S., Efstathiou G., Kaiser N., 1991, *ApJ*, **379**, 440
 Bryan G. L., Norman M. L., 1998, *ApJ*, **495**, 80
 Busch P., White S. D. M., 2017, *MNRAS*, **470**, 4767

⁹ <http://toltec.astro.umass.edu/>

¹⁰ <http://www.ccatobservatory.org/>

- Chadayammuri U., Tremmel M., Nagai D., Babul A., Quinn T., 2020, arXiv e-prints, p. [arXiv:2001.06532](https://arxiv.org/abs/2001.06532)
- Chen H., Avestruz C., Kravtsov A. V., Lau E. T., Nagai D., 2019, *MNRAS*, **490**, 2380
- Chluba J., Nagai D., Sazonov S., Nelson K., 2012, *MNRAS*, **426**, 510
- Chluba J., Switzer E., Nelson K., Nagai D., 2013, *MNRAS*, **430**, 3054
- Cole S., Lacey C. G., Baugh C. M., Frenk C. S., 2000, *MNRAS*, **319**, 168
- Czikon N. G., et al., 2015, *ApJ*, **806**, 18
- Diemer B., 2017, *ApJS*, **231**, 5
- Diemer B., 2018, *ApJS*, **239**, 35
- Diemer B., Kravtsov A. V., 2014, *ApJ*, **789**, 1
- Diemer B., Mansfield P., Kravtsov A. V., More S., 2017, *ApJ*, **843**, 140
- Dietrich J. P., et al., 2019, *MNRAS*, **483**, 2871
- Dolag K., Schindler S., 2000, *A&A*, **364**, 491
- Eckert D., Ettori S., Molendi S., Vazza F., Paltani S., 2013, *A&A*, **551**, A23
- Eckert D., Roncarelli M., Ettori S., Molendi S., Vazza F., Gastaldello F., Rossetti M., 2015, *MNRAS*, **447**, 2198
- Eckert D., et al., 2019, *A&A*, **621**, A40
- Ettori S., Dolag K., Borgani S., Murante G., 2006, *MNRAS*, **365**, 1021
- Ettori S., et al., 2019, *A&A*, **621**, A39
- Flender S., Nagai D., McDonald M., 2017, *ApJ*, **837**, 124
- Fujita Y., Aung H., 2019, *ApJ*, **875**, 26
- Gaskin J. A., et al., 2019, *Journal of Astronomical Telescopes, Instruments, and Systems*, **5**, 021001
- Ghirardini V., et al., 2019, *A&A*, **621**, A41
- Green S. B., Ntampaka M., Nagai D., Lovisari L., Dolag K., Eckert D., ZuHone J. A., 2019, *ApJ*, **884**, 33
- Gunn J. E., Gott J. Richard I., 1972, *ApJ*, **176**, 1
- Hahn O., Martizzi D., Wu H.-Y., Evrard A. E., Teyssier R., Wechsler R. H., 2017, *MNRAS*, **470**, 166
- Hallman E. J., O'Shea B. W., Burns J. O., Norman M. L., Harkness R., Wagner R., 2007, *ApJ*, **671**, 27
- Henden N. A., Puchwein E., Sijacki D., 2019, *MNRAS*, **489**, 2439
- Henson M. A., Barnes D. J., Kay S. T., McCarthy I. G., Schaye J., 2017, *MNRAS*, **465**, 3361
- Hitomi Collaboration et al., 2018, *PASJ*, **70**, 9
- Hoekstra H., Mahdavi A., Babul A., Bildfell C., 2012, *MNRAS*, **427**, 1298
- Hoekstra H., Herbonnet R., Muzzin A., Babul A., Mahdavi A., Viola M., Cacciato M., 2015, *MNRAS*, **449**, 685
- Hojjati A., et al., 2017, *MNRAS*, **471**, 1565
- Iapichino L., Brüggen M., 2012, *MNRAS*, **423**, 2781
- Inogamov N. A., Sunyaev R. A., 2003, *Astronomy Letters*, **29**, 791
- Jiang F., van den Bosch F. C., 2014, *MNRAS*, **440**, 193
- Jiang F., van den Bosch F. C., 2016, *MNRAS*, **458**, 2848
- Käfer F., Finoguenov A., Eckert D., Clerc N., Ramos-Ceja M. E., Sanders J. S., Ghirardini V., 2019, arXiv e-prints, p. [arXiv:1912.01024](https://arxiv.org/abs/1912.01024)
- Kaiser N., 1986, *MNRAS*, **222**, 323
- Kale R., Venturi T., Giacintucci S., Dallacasa D., Cassano R., Brunetti G., Macario G., Athreya R., 2013, *A&A*, **557**, A99
- Kay S. T., Peel M. W., Short C. J., Thomas P. A., Young O. E., Battye R. A., Liddle A. R., Pearce F. R., 2012, *MNRAS*, **422**, 1999
- Khedekar S., Churazov E., Kravtsov A., Zhuravleva I., Lau E. T., Nagai D., Sunyaev R., 2013, *MNRAS*, **431**, 954
- Komatsu E., Seljak U., 2001, *MNRAS*, **327**, 1353
- Komatsu E., Seljak U., 2002, *MNRAS*, **336**, 1256
- Kravtsov A. V., Borgani S., 2012, *ARA&A*, **50**, 353
- Kravtsov A. V., Nagai D., Vikhlinin A. A., 2005, *ApJ*, **625**, 588
- Kravtsov A. V., Vikhlinin A., Nagai D., 2006, *ApJ*, **650**, 128
- Lacey C., Cole S., 1993, *MNRAS*, **262**, 627
- Lau E. T., Kravtsov A. V., Nagai D., 2009, *ApJ*, **705**, 1129
- Lau E. T., Nagai D., Nelson K., 2013, *ApJ*, **777**, 151
- Lau E. T., Nagai D., Avestruz C., Nelson K., Vikhlinin A., 2015, *ApJ*, **806**, 68
- Le Brun A. M. C., McCarthy I. G., Schaye J., Ponman T. J., 2017, *MNRAS*, **466**, 4442
- Lee E., Chluba J., Kay S. T., Barnes D. J., 2019, arXiv e-prints, p. [arXiv:1912.07924](https://arxiv.org/abs/1912.07924)
- Li Y., Mo H. J., Gao L., 2008, *MNRAS*, **389**, 1419
- Mahdavi A., Hoekstra H., Babul A., Bildfell C., Jeltema T., Henry J. P., 2013, *ApJ*, **767**, 116
- Makiya R., Ando S., Komatsu E., 2018, *MNRAS*, **480**, 3928
- Makiya R., Hikage C., Komatsu E., 2019, arXiv e-prints, p. [arXiv:1907.07870](https://arxiv.org/abs/1907.07870)
- Mansfield P., Kravtsov A. V., Diemer B., 2017, *ApJ*, **841**, 34
- Mantz A. B., Allen S. W., Morris R. G., Rapetti D. A., Applegate D. E., Kelly P. L., von der Linden A., Schmidt R. W., 2014, *MNRAS*, **440**, 2077
- Mantz A. B., Allen S. W., Morris R. G., von der Linden A., 2018, *MNRAS*, **473**, 3072
- Marrone D. P., et al., 2012, *ApJ*, **754**, 119
- Maughan B. J., 2007, *ApJ*, **668**, 772
- McCarthy I. G., Schaye J., Bird S., Le Brun A. M. C., 2017, *MNRAS*, **465**, 2936
- McCourt M., Quataert E., Parrish I. J., 2013, *MNRAS*, **432**, 404
- Medezinski E., et al., 2018, *PASJ*, **70**, S28
- Million E. T., Allen S. W., 2009, *MNRAS*, **399**, 1307
- Miyatake H., et al., 2019, *ApJ*, **875**, 63
- Molnar S. M., Hearn N., Haiman Z., Bryan G., Evrard A. E., Lake G., 2009, *ApJ*, **696**, 1640
- Morandi A., Sun M., Forman W., Jones C., 2015, *MNRAS*, **450**, 2261
- More S., Diemer B., Kravtsov A. V., 2015, *ApJ*, **810**, 36
- Motl P. M., Hallman E. J., Burns J. O., Norman M. L., 2005, *ApJ*, **623**, L63
- Mroczkowski T., et al., 2019, *Space Sci. Rev.*, **215**, 17
- Nagai D., 2006, *ApJ*, **650**, 538
- Nagai D., Lau E. T., 2011, *ApJ*, **731**, L10
- Nagai D., Kravtsov A. V., Kosowsky A., 2003, *ApJ*, **587**, 524
- Nagai D., Vikhlinin A., Kravtsov A. V., 2007, *ApJ*, **655**, 98
- Nagarajan A., et al., 2019, *MNRAS*, **488**, 1728
- Navarro J. F., Frenk C. S., White S. D. M., 1997, *ApJ*, **490**, 493
- Nelson K., Rudd D. H., Shaw L., Nagai D., 2012, *ApJ*, **751**, 121
- Nelson K., Lau E. T., Nagai D., Rudd D. H., Yu L., 2014a, *ApJ*, **782**, 107
- Nelson K., Lau E. T., Nagai D., 2014b, *ApJ*, **792**, 25
- Ntampaka M., et al., 2019, *ApJ*, **876**, 82
- Osato K., Flender S., Nagai D., Shirasaki M., Yoshida N., 2018, *MNRAS*, **475**, 532
- Osato K., Shirasaki M., Miyatake H., Nagai D., Yoshida N., Oguri M., Takahashi R., 2020, *MNRAS*, p. 112
- Ota N., Nagai D., Lau E. T., 2018, *PASJ*, **70**, 51
- Parkinson H., Cole S., Helly J., 2008, *MNRAS*, **383**, 557
- Parrish I. J., McCourt M., Quataert E., Sharma P., 2012, *MNRAS*, **419**, L29
- Pike S. R., Kay S. T., Newton R. D. A., Thomas P. A., Jenkins A., 2014, *MNRAS*, **445**, 1774
- Pillepich A., Reiprich T. H., Porciani C., Borm K., Merloni A., 2018, *MNRAS*, **481**, 613
- Plackett R. L., 1950, *Biometrika*, **37**, 149
- Planck Collaboration et al., 2014, *A&A*, **571**, A20
- Planck Collaboration et al., 2018, arXiv e-prints, p. [arXiv:1807.06209](https://arxiv.org/abs/1807.06209)
- Planelles S., Borgani S., Dolag K., Ettori S., Fabjan D., Murante G., Tornatore L., 2013, *MNRAS*, **431**, 1487
- Planelles S., et al., 2017, *MNRAS*, **467**, 3827
- Pratt G. W., Arnaud M., Biviano A., Eckert D., Ettori S., Nagai D., Okabe N., Reiprich T. H., 2019, *Space Sci. Rev.*, **215**, 25
- Raghunathan S., et al., 2019, *ApJ*, **872**, 170
- Rasia E., et al., 2006, *MNRAS*, **369**, 2013
- Rasia E., et al., 2014, *ApJ*, **791**, 96
- Salvati L., Douspis M., Ritz A., Aghanim N., Babul A., 2019, *A&A*, **626**, A27
- Sayers J., et al., 2019, *ApJ*, **880**, 45
- Schneider A., Stoira N., Refregier A., Weiss A. J., Knabenhans M., Stadel J., Teyssier R., 2019, arXiv e-prints, p. [arXiv:1910.11357](https://arxiv.org/abs/1910.11357)
- Sehgal N., et al., 2019, in BAAS. p. 6 ([arXiv:1906.10134](https://arxiv.org/abs/1906.10134))
- Sembolini F., Yepes G., De Petris M., Gottlöber S., Lamagna L., Comis B., 2013, *MNRAS*, **429**, 323
- Sereno M., Ettori S., Moscardini L., 2015, *MNRAS*, **450**, 3649
- Shaw L. D., Nagai D., Bhattacharya S., Lau E. T., 2010, *ApJ*, **725**, 1452
- Shi X., Komatsu E., 2014, *MNRAS*, **442**, 521

- Shi X., Komatsu E., Nelson K., Nagai D., 2015, *MNRAS*, **448**, 1020
- Shi X., Komatsu E., Nagai D., Lau E. T., 2016, *MNRAS*, **455**, 2936
- Shi X., Nagai D., Lau E. T., 2018, *MNRAS*, **481**, 1075
- Shi X., Nagai D., Aung H., Wetzel A., 2020, arXiv e-prints, p. arXiv:2002.00674
- Shirasaki M., Nagai D., Lau E. T., 2016, *MNRAS*, **460**, 3913
- Shirasaki M., Macias O., Ando S., Horiuchi S., Yoshida N., 2019, arXiv e-prints, p. arXiv:1911.11841
- Shirasaki M., Lau E. T., Nagai D., 2020, *MNRAS*, **491**, 235
- Sijacki D., Pfrommer C., Springel V., Enßlin T. A., 2008, *MNRAS*, **387**, 1403
- Simionescu A., et al., 2019a, arXiv e-prints, p. arXiv:1908.01778
- Simionescu A., et al., 2019b, *Space Sci. Rev.*, **215**, 24
- Singh P., Saro A., Costanzi M., Dolag K., 2019, arXiv e-prints, p. arXiv:1911.05751
- Springel V., et al., 2005, *Nature*, **435**, 629
- Sunayama T., More S., 2019, *MNRAS*, **490**, 4945
- Sunyaev R. A., Zeldovich Y. B., 1972, *CoASP*, **4**, 173
- Tashiro M., et al., 2018, in *Proc. SPIE*, p. 1069922, doi:10.1117/12.2309455
- Trac H., Bode P., Ostriker J. P., 2011, *ApJ*, **727**, 94
- Van Waerbeke L., Hinshaw G., Murray N., 2014, *Phys. Rev. D*, **89**, 023508
- Vazza F., Brüggén M., Gheller C., 2013, *MNRAS*, **428**, 2366
- Vazza F., Angelinelli M., Jones T. W., Eckert D., Brüggén M., Brunetti G., Gheller C., 2018, *MNRAS*, **481**, L120
- Ventimiglia D. A., Voit G. M., Donahue M., Ameglio S., 2008, *ApJ*, **685**, 118
- Walker S., et al., 2019, *Space Sci. Rev.*, **215**, 7
- Wik D. R., Sarazin C. L., Ricker P. M., Randall S. W., 2008, *ApJ*, **680**, 17
- Xhakaj E., Diemer B., Leauthaud A., Wasserman A., Huang S., Luo Y., Adhikari S., Singh S., 2019, arXiv e-prints, p. arXiv:1911.09295
- Yu L., Nelson K., Nagai D., 2015, *ApJ*, **807**, 12
- Zhang Y.-Y., et al., 2010, *ApJ*, **711**, 1033
- Zhao D. H., Jing Y. P., Mo H. J., Börner G., 2009, *ApJ*, **707**, 354
- Zhuravleva I., Churazov E., Kravtsov A., Lau E. T., Nagai D., Sunyaev R., 2013, *MNRAS*, **428**, 3274
- Zhuravleva I., et al., 2014, *Nature*, **515**, 85
- Zu Y., Mandelbaum R., Simet M., Rozo E., Rykoff E. S., 2017, *MNRAS*, **470**, 551
- da Silva A. C., Kay S. T., Liddle A. R., Thomas P. A., 2004, *MNRAS*, **348**, 1401
- van den Bosch F. C., 2002, *MNRAS*, **331**, 98
- van den Bosch F. C., Jiang F., Hearin A., Campbell D., Watson D., Padmanabhan N., 2014, *MNRAS*, **445**, 1713
- von der Linden A., et al., 2014, *MNRAS*, **443**, 1973

APPENDIX A: CONVERTING BETWEEN DEX AND PERCENT SCATTER

Consider a sample of observed and predicted quantities, denoted X_{true} and X_{pred} , respectively. The residual is defined as $\Delta X = X_{\text{pred}} - X_{\text{true}}$ and the base-10 logarithmic residual is defined as $\mathcal{R} = \log(X_{\text{pred}}) - \log(X_{\text{true}}) = \log(X_{\text{pred}}/X_{\text{true}})$. The standard deviation of \mathcal{R} is

$$\sigma_{\mathcal{R}} = \sqrt{\frac{1}{N-1} \sum_{i=1}^N (\mathcal{R}_i - \bar{\mathcal{R}})^2} \approx \sqrt{\frac{1}{N-1} \sum_{i=1}^N \left(\log \left[\frac{X_{\text{pred},i}}{X_{\text{true},i}} \right] \right)^2}, \quad (\text{A1})$$

where the approximation is due to the fact that, for an unbiased estimator, the bias $\bar{\mathcal{R}} \approx 0$. This quantity, $\sigma_{\mathcal{R}}$, is referred to as the ‘‘scatter’’ and is in units of decimal exponent (dex).

For relatively small log-residuals (i.e., on the order of 0.1 dex), the Taylor expansion of the natural logarithm gives that

$$\log(X_{\text{true}}/X_{\text{pred}}) = \frac{\ln(X_{\text{true}}/X_{\text{pred}})}{\ln(10)} \approx \frac{1}{\ln(10)} \left[\frac{X_{\text{true}}}{X_{\text{pred}}} - 1 \right]. \quad (\text{A2})$$

Note that $(\log[X_{\text{pred}}/X_{\text{true}}])^2 = (\log[X_{\text{true}}/X_{\text{pred}}])^2$. The standard deviation of the residuals is

$$\sigma_{\Delta X} \approx \sqrt{\frac{1}{N-1} \sum_{i=1}^N (X_{\text{true},i} - X_{\text{pred},i})^2}, \quad (\text{A3})$$

where the approximation is again due to the assumption of negligible bias. Since we are interested in the scatter in the observed quantity at fixed independent variables (e.g., the scatter in Y_{SZ} at fixed mass), we compute the fractional scatter $\sigma_{\Delta X}/X = \sigma_{\Delta X}/X_{\text{pred}}$. Hence, we find that

$$\begin{aligned} \frac{\sigma_{\Delta X}}{X} &\approx \sqrt{\frac{1}{N-1} \sum_{i=1}^N \left(\frac{X_{\text{true},i} - X_{\text{pred},i}}{X_{\text{pred},i}} \right)^2} \\ &\approx \ln(10) \sqrt{\frac{1}{N-1} \sum_{i=1}^N \left(\log \left[\frac{X_{\text{pred},i}}{X_{\text{true},i}} \right] \right)^2} = \ln(10) \sigma_{\mathcal{R}}. \end{aligned} \quad (\text{A4})$$

Thus, the base-10 log-residual scatter can be converted to fractional scatter by multiplying by $\ln(10) \approx 2.3$. Since this conversion uses the approximation of the natural logarithm’s Taylor expansion, it is accurate to 4% (12%) for $\sigma_{\mathcal{R}} \lesssim 0.1$ (0.2) dex.

A consequence of the above is that the scatter in the base-10 log-residuals is an approximation of the fractional scatter. Unfortunately, this has led to some confusion in the literature, specifically in regards to reports of the scatter in observable-mass relations. For example, Sembolini et al. (2013) and Planelles et al. (2017) compute scatter using base-10 logarithms (i.e., $\sigma_{\mathcal{R}}$ in dex) and report these values as percentages without proper conversion via multiplication by $\ln(10)$. As a consequence, their reported scatter percentages are systematically less than those reported in the bulk of the other simulation literature (see Section 3.3) by roughly a factor of 2 – 2.5. Such mistakes are common; thus, we hope that the above discussion helps to reduce the frequency of such errors in future studies.

APPENDIX B: THE EFFECT OF THE MASS CUTOFF

The level of variation in the slope and scatter of the $Y_{\text{SZ}} - M$ relation caused by changes in the cosmology (see Fig. 7) are similar in magnitude to the level of variation imparted due to changing the minimum halo mass cutoff. In particular, decreasing the minimum halo mass used to compute these relations tends to decrease the overall scatter in the $Y_{\text{SZ}} - M$ relation due to the heteroscedasticity discussed in Section 2.5 and, in addition, tends to move its slope closer towards self-similarity due to the decrease in f_{nth} with decreasing halo mass. As demonstrated in Fig. B1, decreasing the mass cutoff from $\log(M_{200\text{m}}/[h^{-1}M_{\odot}]) \geq 14$ to $\log(M_{200\text{m}}/[h^{-1}M_{\odot}]) \geq 12$ decreases the percent scatter in $Y_{\text{SZ}}(< R_{\text{ap}}) - M(< r_{\text{ap}})$ by $\sim 1\%$ (in absolute units, not relative) and increases its slope by ~ 0.01 towards self-similarity. While these changes are small, this does impart a degeneracy between the mass regime used and the cosmological parameters that may become important with sufficiently large cluster samples. As a caveat, we emphasize that our model does not include various physical sources of non-thermal pressure support that become increasingly important for low-mass haloes (e.g., feedback). In addition, it remains unclear how valid our choice of gas density normalization (i.e., fixed $M_{\text{gas}}(< 2r_{200\text{m}})/M(< 2r_{200\text{m}}) = \Omega_{\text{b}}/\Omega_{\text{m}}$) is for low-mass haloes. Hence, these trends with respect to halo mass must be considered with some reservation.

This paper has been typeset from a $\text{\TeX}/\text{\LaTeX}$ file prepared by the author.

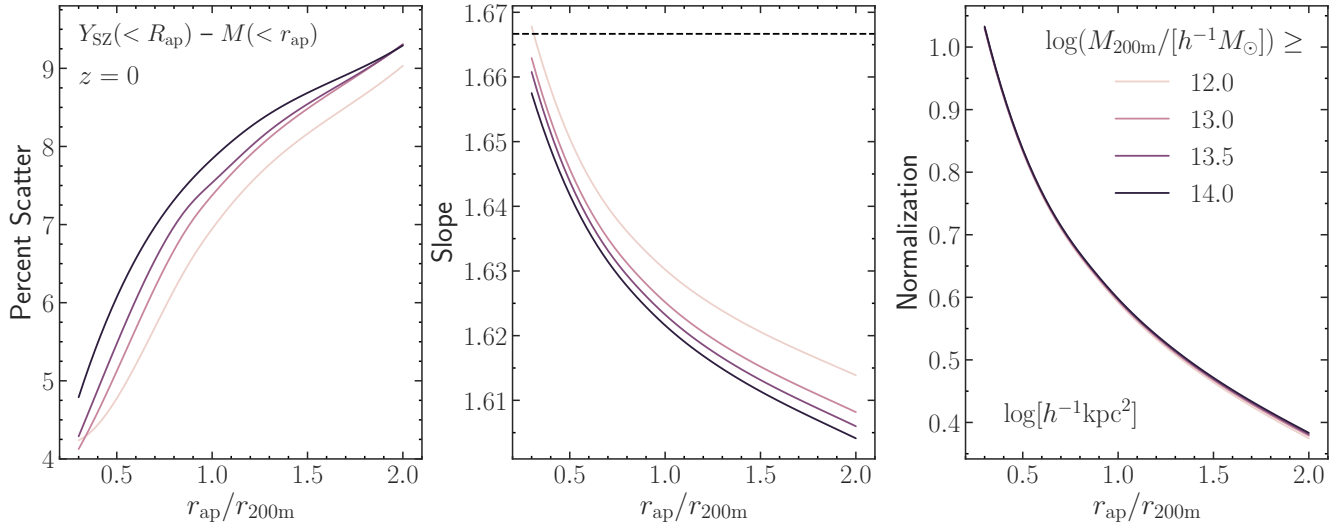


Figure B1. The best fit normalization, slope, and percent scatter of the $Y_{\text{SZ}}(< R_{\text{ap}}) - M(< r_{\text{ap}})$ relation at $z = 0$. The fit parameters are shown as a function of r_{ap} and different curves illustrate the effect of changing the low-mass cutoff for haloes included in the relation, with a fixed high-mass cutoff of $\log(M_{200\text{m}}/[h^{-1}M_{\odot}]) \leq 15.6$. As lower mass haloes are included in the fit, the overall scatter decreases slightly and the slope increases slightly towards self-similarity, regardless of r_{ap} . The implied heteroscedasticity is due to the increase in MAR variance with increasing halo mass (see Fig. 2) combined with a correlation between non-thermal pressure support and MAR. The decrease of the slope with increasing cutoff mass implies that $f_{\text{nth}}(r)$ grows more rapidly with mass for higher mass haloes than for lower-mass haloes, resulting in further deviation from self-similar scaling when the low-mass haloes are excluded.